Athens Journal of Sciences - Volume 13, Issue 1, March 2026 – Pages 65-98

Mapping Hydrothermal Alteration Minerals using Landsat 8 and ASTER Data: A Case Study from the Red Sea Hills, NE Sudan

By Mohammed Abdulrauf Mohammed Ibrahim[*] & Evangelos Papadimitriou[±]

Hydrothermal alteration minerals provide key indicators for mineral exploration, particularly in arid and inaccessible regions where field surveys are constrained. This study integrates remote sensing and GIS techniques to map alteration zones in the Red Sea Hills, NE Sudan, using Landsat 8 OLI and ASTER datasets. Preprocessing included FLAASH atmospheric correction and Minimum Noise Fraction (MNF) transformation to enhance spectral integrity. For Landsat 8 diagnostic band ratios and density slicing were applied to highlight ferric/ferrous iron oxides and clay/hydroxyl-bearing minerals, followed by supervised Parallelepiped classification of Sabins band ratios and Crosta transformations to delineate prospective alteration zones. ASTER VNIR-SWIR data enabled higher resolution mapping through Mineral Indices and Spectral Angle Mapper (SAM) classification against USGS spectral library endmembers. These approaches revealed three principal hydrothermal alteration zones: phyllic (muscovite, illite), argillic (kaolinite, alunite), and propylitic (epidote, chlorite). Results demonstrate that Landsat 8 is effective for regional-scale reconnaissance, but ASTER's superior spectral resolution provides more accurate and mineralogically de-tailed alteration mapping. The study underscores the value of ASTER data for early-stage exploration in structurally complex, mineralized terranes such as the Arabian-Nubian Shield.

Keywords: *Hydrothermal alteration; Mineral exploration; ASTER; Landsat 8; Crosta; Band Ratio; Spectral indices; SAM classification; Arabian-Nubian Shield*

Introduction

Remote sensing data from the multispectral Landsat 8 OLI (LC8) and the semi-hyperspectral ASTER (AST) sensors play an important role in locating mineral deposits and in reducing the costs associated with prospecting and exploration (Crósta and Moore 1989, Debba et al. 2005, Carrino et al. 2015, Amer et al. 2016, Alimohammadi et al. 2015). Although commercial mineral deposits are limited in their genetic types and modes of occurrence, a wide range of geological criteria and indicators have been established to support remote sensing techniques in identifying these deposits. These indicators, observable in spaceborne and aerial imagery, include lithological features, rock alteration patterns, structural controls, and geobotanical evidence (Hunt 1979, Hunt and Ashley 1979, Gupta 2017).

Hydrothermal deposits typically form at shallow crustal depths, ranging from approximately 2 to 6 km below the surface. They are usually associated with extensive

[*]Faculty of Petroleum and Minerals, Al Neelain University, Sudan.
[±]Marine Operations Manager, Leaf Global Environmental Services PLC, Saudi Arabia.

https://doi.org/10.30958/ajs.13-1-3 doi=10.30958/ajs.13-1-3

hydrothermal alteration (HA), which is zonal in nature. This zonation progresses outward and upward from an inner potassic zone, characterized by intense alteration and dominated by biotite and K-feldspar, into phyllic, argillic, and finally propylitic zones (Mars and Rowan 2006, Berger et al. 2014). The phyllic zone commonly consists of sericite and pyrite-rich rocks, while the ore zone includes disseminated chalcopyrite, molybdenite, pyrite, and other sulfide minerals. Much of the ore is concentrated near the boundary between the potassic and phyllic zones, often forming a cylindrical ore shell. The argillic zone is composed of rocks enriched in alunite and kaolinite, whereas the outer propylitic zone consists of weakly altered rocks with variable mineralogy, including chlorite, epidote, and calcite (Spatz et al. 1995, Seedorff et al. 2005, Mars and Rowan 2006). These successive alteration zones (AZs), rich in characteristic minerals, provide an essential reference for mapping HA using both LC8 and AST data (Pour et al. 2018, Pour et al. 2019).

In Sudan, several studies have successfully applied multispectral data from Landsat TM, ETM+, and LC8 sensors to delineate gossans, gold-bearing zones, and as-sociated sulfide mineralization. These studies have been guided by the distinct spectral signatures of gossans and AZs related to mineral deposits (Zeinelabdein and Albiely 2008, Abdelsalam et al. 2000, El Khidir 2006, El Khidir and Babikir 2013). The Gebeit area was selected as the study site due to the lack of availability of previous information, particularly from remote sensing investigations using LC8 and AST data. In addition, the region holds significant economic importance as an active and prospective mining area.

In this study, LC8 data, processed using various digital image processing algorithms and validated with spectral analysis of AST data, were used to delineate and map the AZs of hydrothermal minerals associated with gold-bearing sulfide deposits.

Geological Setting

The Red Sea Hills (RSHs) of Sudan form part of the Nubian Shield, which belongs to the Arabian-Nubian Shield (ANS) of northeastern Africa and the western Arabian Peninsula. The ANS extends along both sides of the RSHs, from Egypt in the northwest, the Sinai Peninsula in the north, and Saudi Arabia in the northeast, to Ethiopia and Yemen in the southwest and southeast, respectively (Johnsonet al. 2004, Johnson et al. 2011). The ANS is recognized as one of the major orogenic belts formed during the Neoproterozoic assembly of Greater Gondwana. It represents an accretionary orogenic belt composed predominantly of juvenile intra-oceanic island arcs, oceanic islands, and microcontinental fragments (Stern 1994). The ANS evolved between 900 and 550 Ma as a result of the closure of the Mozambique Ocean (800-650 Ma) and the subsequent collision between East and West Gondwana (Stern 1994, Stern 2002). Kröner et al. (1987) divided the RSHs into five geologically distinct terranes, separated from each other by ophiolite-decorated suture zones.

The study area is located within the Gebeit Terrane (Figure 1), which comprises arc-related, low-grade volcano-sedimentary sequences and syn-tectonic igneous complexes in the area north of the Nakasib Suture (Vail 1985, Klemenic and Poole 1988). Whole rock Rb/Sr isochron ages of approximately 720 Ma have been reported

for volcanic and plutonic rocks within the terrane (Fitches et al. 1983, Almond and Ahmed 1987). Regionally, major ductile shearing, faulting, and compressional forces acting from the east to southeast are interpreted to have generated the dominant NE-trending structural fabric of the RSHs, including folds and faults, associated with ophiolite-decorated suture zones such as the Nakasib Suture (Almond and Ahmed 1987, Abdelsalam 2010). Younger NW-trending strike-slip shear zones, including Oko and Keraf shear zones, deform older these earlier structures like Nadasib suture (Abdelsalam 2010).

Figure 1: *Terranes and Suture Zones of the ANS, illustrating the Predominant Ages of Arc Magmatism within each Terrane and the Location of the Study Area*

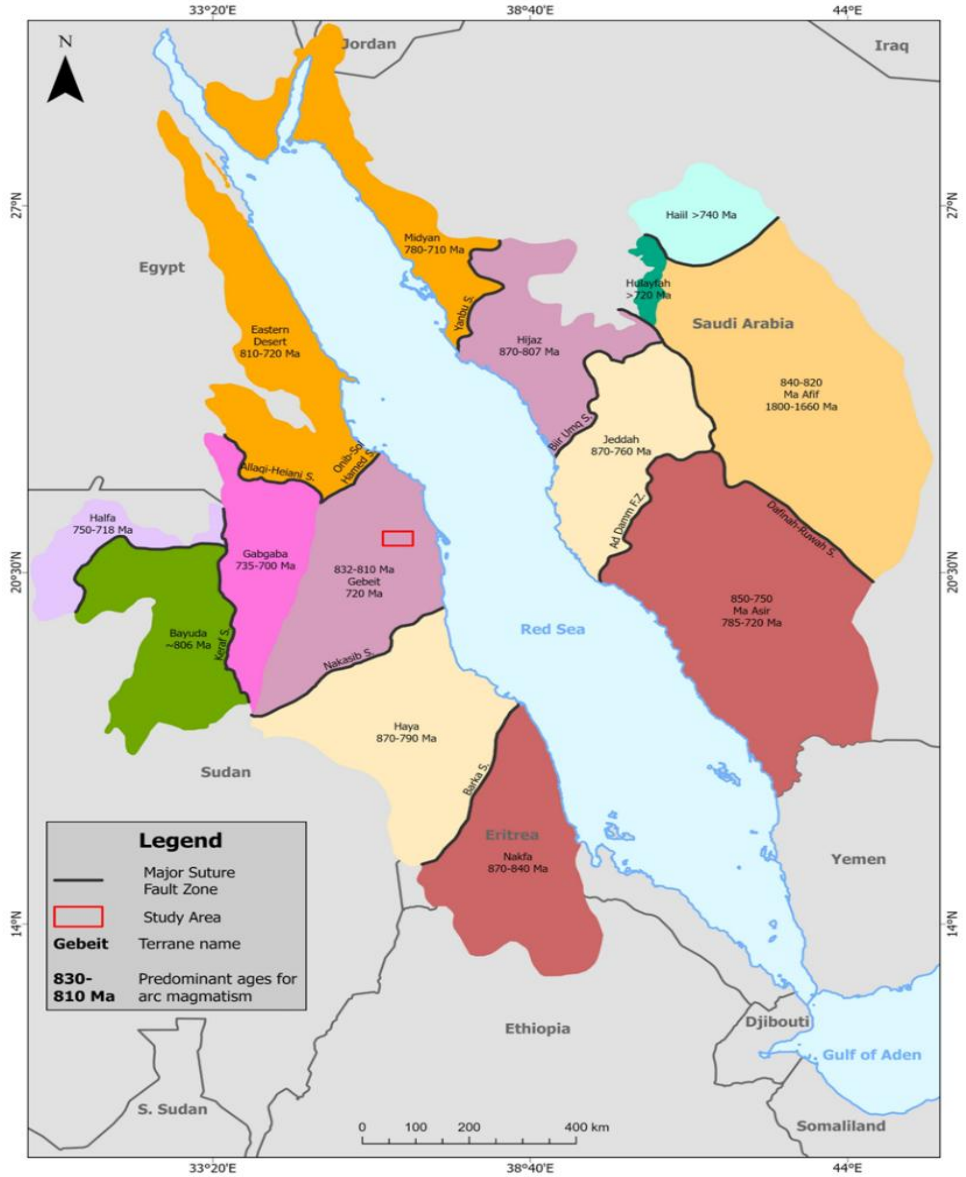

Source: Modified after (Abdelsalam, 2010).

Materials and Methods

Image Data and Data Preprocessing

Landsat 8 OLI Data

LC8 was launched on an Atlas V rocket from Vandenberg Air Force Base, California, USA, on February 11, 2013. It is the eighth satellite in the Landsat program, which has been continuously operated since the 1970s as a joint initiative between the U.S. Geological Survey (USGS) and NASA (Roy et al. 2014, Blondes et al. 2016). LC8 carries two primary instruments: the OLI (Operational Land Imager), which acquires data in nine spectral bands spanning the visible (Table 1), NIR (near-infrared), and SWIR (shortwave infrared) regions (including a panchromatic band and a cirrus band), and the TIRS (Thermal Infrared Sensor), which records two longwave thermal bands (bands 10 and 11) (Wulder et al. 2008, Roy et al. 2014, Blondes et al. 2016).

In this study, a single optical multispectral LC8 scene was used, corresponding to path 172, row 45, acquired on June 5, 2025. The dataset was downloaded from the USGS EROS (Earth Resources Observation and Science) Center website.

ASTER Data

ASTER (Advanced Spaceborne Thermal Emission and Reflection Radiometer) is a multispectral sensor with high spatial, spectral, and radiometric resolution (Abrams, Hook and Ramachandran, 2002). AST data are recorded in 14 spectral bands using three subsystems: the VNIR (Visible and Near Infrared) subsystem, consisting of three bands with wavelengths from (0.52 to 0.86 μm) at 15 m spatial resolution; the SWIR (Shortwave Infrared) subsystem, comprising six bands with wavelengths from (1.6 to 2.43 μm) at 30 m spatial resolution; and the TIR (Thermal Infrared) subsystem, which includes five bands (Bands 10-14) spanning (8.125-11.65 μm) at 90 m spatial resolution (Table 1). The instrument also has a long-track stereo capability, and each AST scene covers an area of 60 × 60 km², making it particularly suitable for regional mapping (Yamaguchi et al., 1999; Abrams, 2000; Yamaguchi et al., 2001; Abrams, Hook and Ramachandran, 2002).

For this research, one AST scene was used. The dataset (Scene ID: 00303032008081257) was acquired on August 12, 2008, and downloaded from the NASA Earthdata Search portal.

Table 1. *Overview of LC8 and AST Imaging Bands*

Satellite	Band No.	Covered Spectrum	Wavelength (μm)	Resolution (m)
LC8	1	Coastal/Aerosol	0.43-0.45	30
LC8	2	Blue	0.45-0.51	30
LC8	3	Green	0.53-0.59	30
LC8	4	Red	0.64-0.67	30
LC8	5	NIR	0.85-0.88	30
LC8	6	SWIR 1	1.57-1.65	30
LC8	7	SWIR 2	2.11-2.29	30
LC8	8	Panchromatic	0.50-0.68	15
LC8	9	Cirrus	1.36-1.38	30
AST	1	VNIR	0.52 - 0.60	15

AST	2	VNIR	0.63 - 0.69	15
AST	3N	VNIR	0.78 - 0.86	15
AST	3B	VNIR	0.78 - 0.86	15
AST	4	SWIR	1.600 - 1.700	30
AST	5	SWIR	2.145 - 2.185	30
AST	6	SWIR	2.185 - 2.225	30
AST	7	SWIR	2.235 - 2.285	30
AST	8	SWIR	2.295 - 2.365	30
AST	9	SWIR	2.360 - 2.430	30
AST	10	TIR	8.125 - 8.475	90
AST	11	TIR	8.475 - 8.825	90
AST	12	TIR	8.925 - 9.275	90
AST	13	TIR	10.25 - 10.95	90
AST	14	TIR	10.95 - 11.65	90

Source: Compiled from USGS Landsat 8 and NASA ASTER specifications

Software

Image processing was performed using ENVI (Environment for Visualizing Images) version 5.3 and ArcGIS version 10.8, installed on a high-performance computer. These software packages provided the necessary tools for preprocessing, spectral analysis, and spatial data integration.

Data Preprocessing

The LC8 data were geometrically corrected and georeferenced by the USGS prior to download. The data are provided in the UTM (Universal Transverse Mercator) coordinate system, zone 36N, based on the WGS84 datum, with all units expressed in meters. Atmospheric correction was carried out using the FLAASH (Fast Line-of-sight Atmospheric Analysis of Spectral Hypercubes) model (Fraser and Green 1987). To improve signal quality and computational efficiency, the MNF (Minimum Noise Fraction) transformation was applied, enabling dimensionality reduction, noise segregation, and optimization for subsequent image analysis (Cooley et al. 2002, Shnain et al. 2024).

Similarly, the AST data underwent atmospheric correction using the FLAASH technique, followed by post-processing band math to remove negative values. To enhance comparability, the six SWIR bands (30 m resolution) were resampled to match the three VNIR bands (15 m resolution), resulting in a nine-band semi-hyperspectral dataset with a uniform spatial resolution of 15 m (Shnain et al., 2024).

Landsat 8 OLI Data for Mineral Prospecting

LC8 data are considered fundamental for mineral prospecting, especially in remote or inaccessible regions. They are extremely useful during the systematic exploration phase of mining and are widely applied to geological mapping and mineral exploration worldwide (Safari et al. 2018, Mwaniki et al. 2015). The LC8 spectral range (0.325–2.5 μm) records solar-reflected light and includes several diagnostic absorption features of alteration minerals. These features are related to vibrational overtones, electronic transitions, charge transfer, and conduction processes (Sabins and Lulla 1987).

In this study, LC8 data were processed using two complementary approaches: (i) the Band Ratio (BR) technique, and (ii) Supervised Classification applied to Sabins BR and to the Feature Oriented Principal Component Selection (FOPCS) method. Both approaches were used to delineate HA zones (Sabins and Lulla, 1987).

The Band Ratio Process for Mineral Prospecting

BR is one of the most effective techniques for detecting alteration minerals such as ferrous and ferric iron oxides, as well as hydroxyl-bearing minerals (Sabins and Lulla 1987, Zhang et al. 2007). BR images are generated by dividing the digital number (DN) values of one spectral band by those of another (Sabins 1999, Lillesand et al. 2015). These images enhance spectral differences between minerals, minimize the influence of topography and solar illumination, and highlight absorption features associated with alteration. Gray-scale ratio images display pixels with the largest differences in reflectance between two bands. BRs are therefore widely used to emphasize iron oxide and clay or hydroxyl-bearing minerals, which are critical indicators of HA (Gupta 2017). To further enhance interpretation, density slicing was applied, converting the continuous tonal variations of the ratio images into discrete intervals corresponding to specified DN ranges (Sabins and Lulla 1987, Zhang et al. 2007).

Supervised Classification

Supervised classification is another powerful remote sensing technique for mapping mineral AZs. It involves the selection of sample Regions of Interest (ROIs) and the extraction of their spectral signatures across all bands. These signatures are used to compute statistical parameters that guide classification algorithms. In this study, the Parallelepiped classifier was used to assign each pixel to the most probable class, enabling accurate and detailed thematic mapping (Richards 2022, Lillesand et al. 2015). Supervised classification was applied to false-color composite (FCC) images generated from Sabins BR and from the FOPCS method to identify HA zones.

Sabins Band Ratio FCC Image

The Sabins FCC image was produced by assigning BR of 6/7, 4/6, and 4/2 to the red, green, and blue channels, respectively (Sabins 1999). This combination enhances the spectral expression of alteration minerals. The 6/7 ratio highlights clay-rich zones, since clay minerals show strong reflectance in Band 6 (SWIR1) and low reflectance in Band 7 (SWIR2), which appear reddish in the composite. The 4/2 ratio enhances iron oxide-bearing areas, reflecting the absorption features in the blue region (Band 2) and the high reflectance in the red region (Band 4). These spectral properties allow iron-bearing minerals to be clearly distinguished (Pour and Hashim 2012a, 2012b).

The FOPCS (Feature Oriented Principal Component Selection) process

The FOPCS method, also referred to as the Crosta technique, is a targeted principal component analysis (PCA) approach that uses only a subset of bands selected to emphasize spectral features of interest (Crósta 1989, Loughlin 1991, Crósta et al. 2003). In this study, two band combinations were analyzed: the H-image, designed to

enhance hydroxyl-bearing and clay minerals, and the F-image, intended to highlight iron oxide signatures. The eigenvector loadings of the resulting principal components were carefully examined to determine which components best represent the spectral properties of alteration minerals (Zhang et al. 2007).

ASTER Data for Mineral Prospecting

AST data, with their high spatial and spectral resolution, provide valuable coverage for identifying HA minerals and lithological units (Cooley et al. 2002). HA zones such as phyllic, argillic, and propylitic can be distinguished by their characteristic absorption features within AST's spectral range. Specifically, the phyllic alteration zone, dominated by illite and muscovite (sericite), is characterized by a strong Al-OH absorption feature centered at 2.20 μm, which coincides with AST Band 6. The argillic zone, comprising kaolinite and alunite, shows a secondary Al-OH absorption feature at 2.17 μm, corresponding to AST Band 5. The propylitic zone, characterized by chlorite and epidote, exhibits absorption features near 2.35 μm, coinciding with AST Band 8 (Mars and Rowan 2006, Pour et al. 2018, Testa et al. 2018).

In the present study, AST VNIR - SWIR data were analyzed using two methods: mineral indices derived from BR and the SAM classifier. Both approaches were applied to detect (illite, muscovite, kaolinite, alunite, epidote, and chlorite) which are diagnostic minerals of (phyllic, argillic, and propylitic) AZs.

Mineral Indices

Mineral indices were calculated by applying specific BR that target diagnostic absorption features of selected minerals (Rowan and Mars 2003, Rowan et al. 2003). Preprocessing of the AST dataset included radiometric calibration and atmospheric correction of VNIR and SWIR bands. Lithological indices were also derived for the TIR bands, based on the distinct spectral properties of various minerals and rock types (Ninomiya, 2003; Van der Meer et al., 2012).

Three indices were particularly applied in this study:

$$\text{Muscovite Index} = \frac{Band\ 7}{Band\ 6}$$

$$\text{Alunite Index} = \frac{Band\ 7}{Band\ 5} \times \frac{Band\ 7}{Band\ 8}$$

$$Kaolinite\ Index = \frac{Band\ 4}{Band\ 5} \times \frac{Band\ 8}{Band\ 6}$$

Spectral Angle Mapper (SAM) Classifier

The SAM technique classifies pixels based on their spectral similarity to known reference spectra (Rajendran et al. 2013). Each pixel's spectral vector is compared to library spectra of known minerals, and the similarity is quantified by measuring the angle between the vectors. Smaller angles indicate greater similarity. This procedure produces a spectral similarity map, in which each pixel is classified according to its closest match from the spectral library. The SAM output includes a classified image displaying the distribution of alteration minerals and rule images

showing the angular distance (in radians) between pixel spectra and reference spectra (Kruse et al. 1993, Rowan and Mars 2003, Van der Meer et al. 2012).

Figure 2. *Two-dimensional Illustration of Spectral Vectors r (reference spectrum) and n (pixel spectrum), showing the Spectral Angle (a) between them*

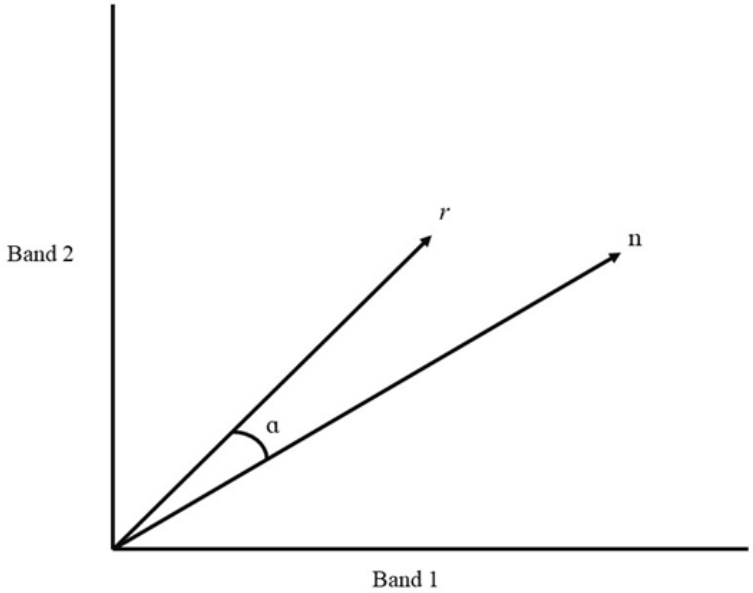

Source: Modified after (Kruse et al., 1993).

Results

Landsat 8 OLI Data Processing for Mineral Prospecting

Multispectral LC8 data were processed to delineate and map AZs associated with mineralization. These zones are defined by the presence of key alteration minerals, including ferric and ferrous iron oxides such as hematite, goethite, and limonite, as well as clay and hydroxyl-bearing minerals such as kaolinite, montmorillonite, illite, and alunite. The diagnostic spectral features of these minerals serve as important indicators for identifying potential mineral deposits within a multispectral remote sensing framework. To avoid misinterpretation, alluvial wadi deposits were masked during the analysis, since they often contain weathered, altered, and fragmented rock material whose spectral signatures can obscure or distort the signals of the targeted alteration minerals.

Band Ratio Images

Selective BR were applied to highlight HA zones. Ratios 4/2, 6/5, and 6/7 were specifically used to identify ferrous iron oxides, ferric iron oxides, and hydroxyl-bearing minerals, respectively. A low-pass filter was first applied to the ratio images to reduce noise. The resulting grayscale images were further enhanced through density slicing, which emphasized the spectral responses associated with the target

minerals. Finally, the density-sliced results were converted into vector classes, allowing the delineation and mapping of distinct AZs.

Ferrous Iron Oxides and Ratio

Ferrous iron oxides are characterized by high reflectance in the red portion of the spectrum (Band 4) and low reflectance in the blue region (Band 2) of LC8 data. For this reason, BR of 4/2 was used to delineate areas enriched in ferrous iron oxides. In the grayscale display, ferrous-rich areas appear in light tones, while in the density-sliced output they are highlighted in red (Figure 3a, b).

Figure 3. *BR 4/2 Image used for mapping Ferrous Oxides: (A) Grayscale Display, where High Values appear as Bright Tones; (B) Density-sliced Display, where High Values are highlighted in Red*

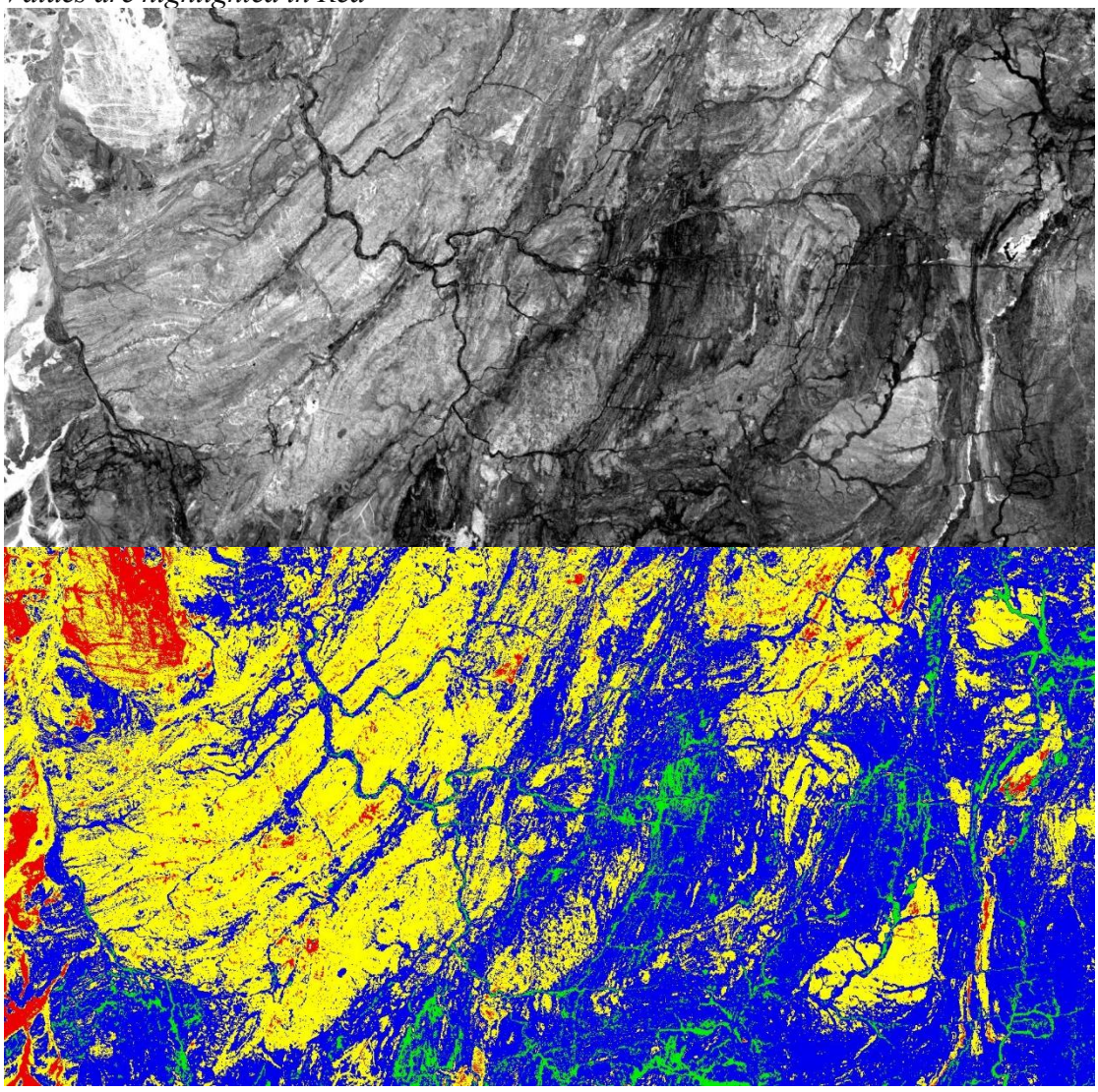

Source: Authors own elaboration

Ferric Iron Oxides Band Ratio

Ferric iron oxides show diagnostic absorption in the near-infrared region (Band 5) and high reflectance in the shortwave infrared region (Band 6). Consequently, the BR 6/5 effectively delineates ferric oxide-rich areas. These appear in light tones in the grayscale image and are displayed in red hues in the density-sliced image (Figure 4a, b).

Figure 4. *BR 6/5 Image used for mapping Ferric Oxides: (A) Grayscale Display, where High Values ap-pear as Bright Tones; (B) Density-sliced Display, where high values are highlighted in Red*

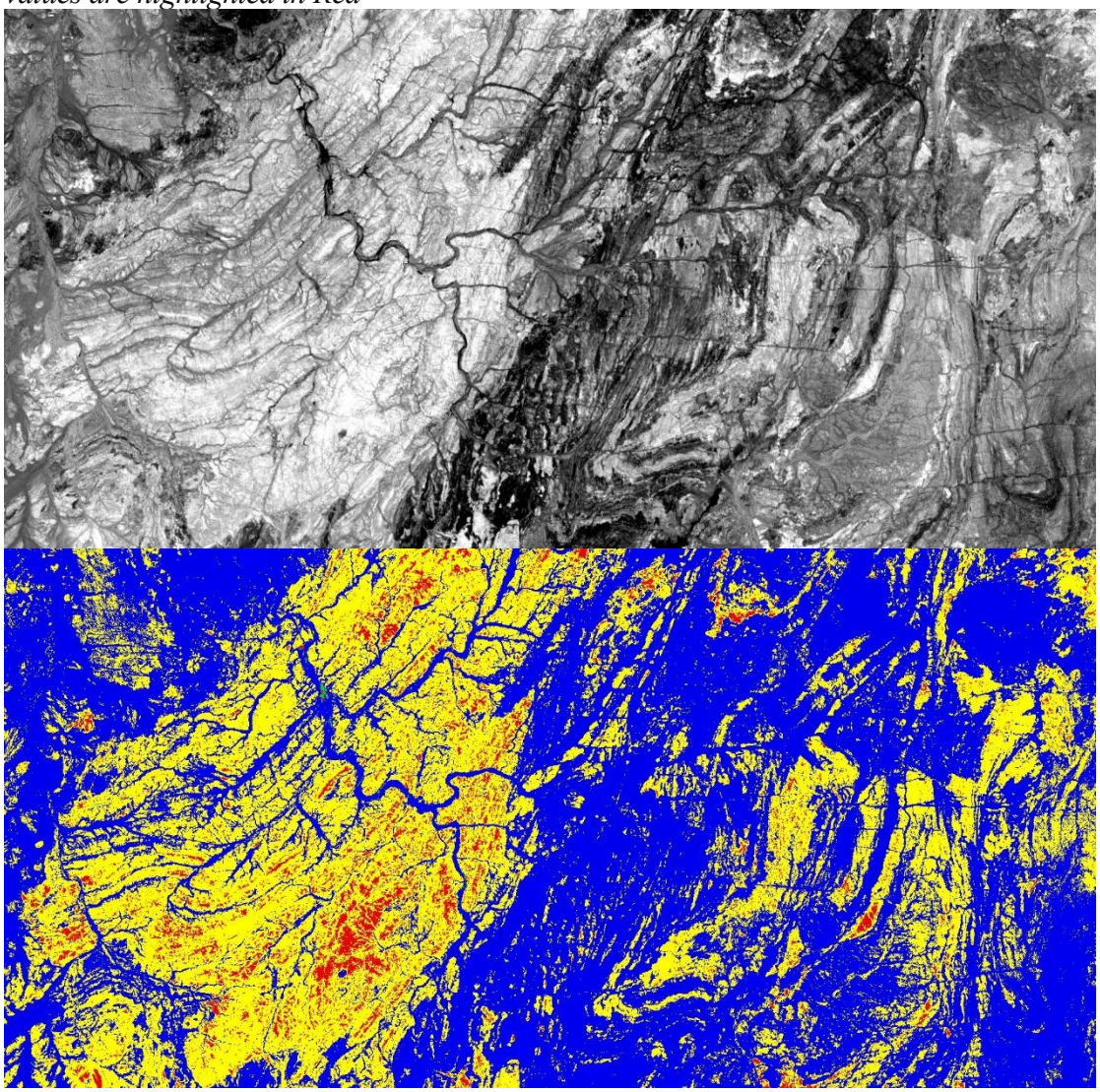

Source: Authors own elaboration

Hydroxyl Bearing Band Ratio

Hydroxyl-bearing alteration minerals, including clays, micas, and amphiboles, exhibit distinct absorption features in the SWIR-2 region (Band 7) due to the strong Al - OH and Mg-OH vibrational absorptions. At the same time, they show high reflectance in the SWIR-1 region (Band 6). Accordingly, BR of 6/7 was used to identify hydroxyl-bearing mineral assemblages. In the outputs, these zones appear in bright tones in the grayscale image and in red hues in the density-sliced version (Figure 5a, b).

Figure 5. *BR 6/7 Image used for Mapping Clay Minerals: (A) Grayscale Display, where High Values appear as Bright Tones; (B) Density-sliced display, where High Values are highlighted in Red*

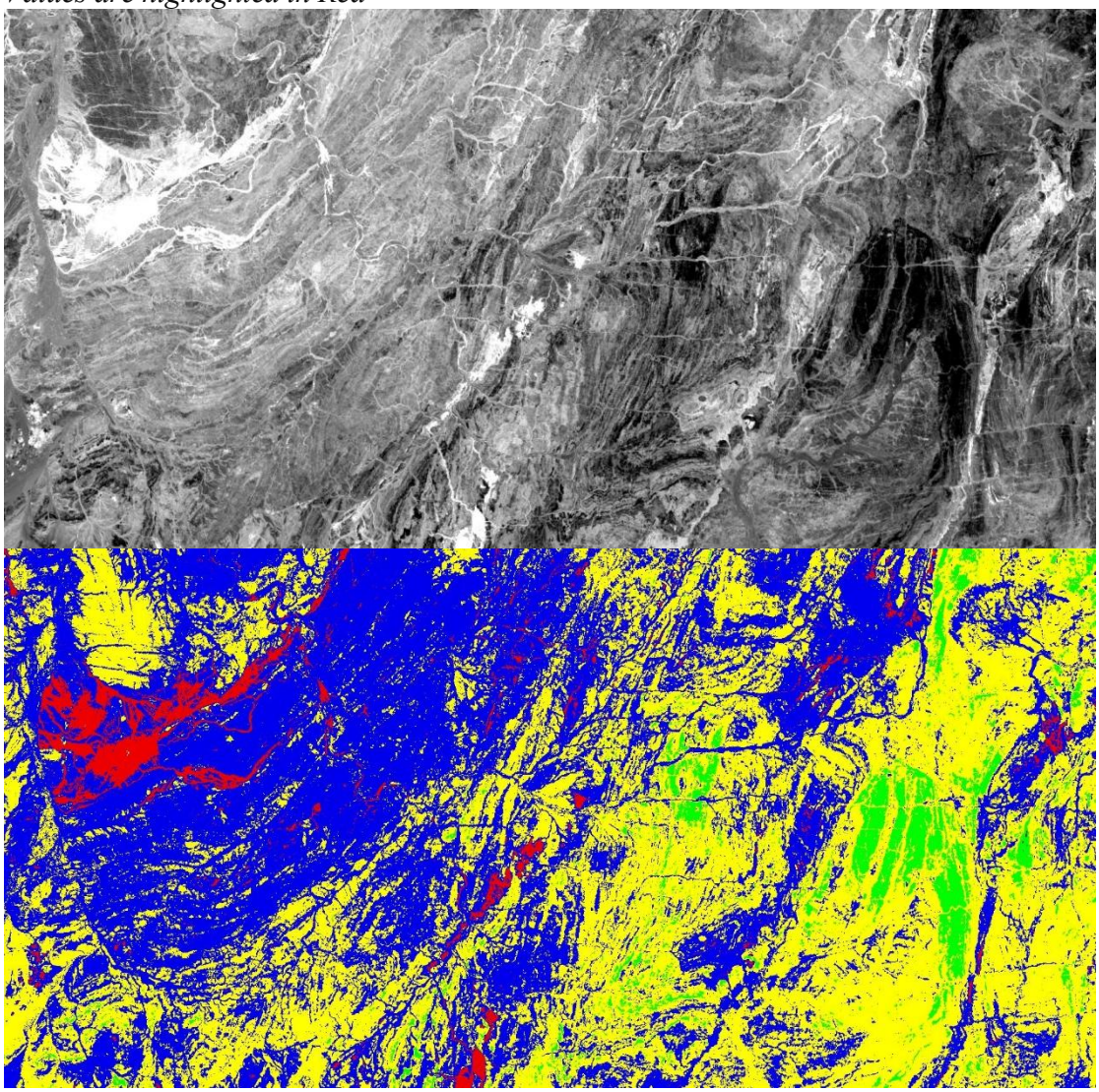

Source: Authors own elaboration

GIS Spatial Analysis

The BR images derived from ratios 4/2, 6/5, and 6/7 revealed three distinct types of potential AZs. Each was extracted as a separate class through density slicing and subsequently converted into vector format within a GIS environment. As shown in Figure 6a, ferrous oxide zones are represented in blue, ferric oxide zones in green, and clay-rich (hydroxyl-bearing) zones in red. To identify the most prospective zones of HA, a spatial intersection analysis was carried out. This procedure highlighted the areas of overlap among the three classes, rep-resenting the zones with the highest probability of being associated with hydrothermal mineralization. These priority targets are displayed in yellow in Figure 6b.

Figure 6. *(a) AZs Overlaid on the Satellite Image, showing High Values of the BR Images: 6/7 for Clay Minerals (red), 4/2 for Ferrous Oxides (blue), and 6/5 for Ferric Oxides (green). (b) Spatial Intersection Analysis of the vectorized Anomalous Values from the BR, highlighting the overlapping AZs in Yellow*

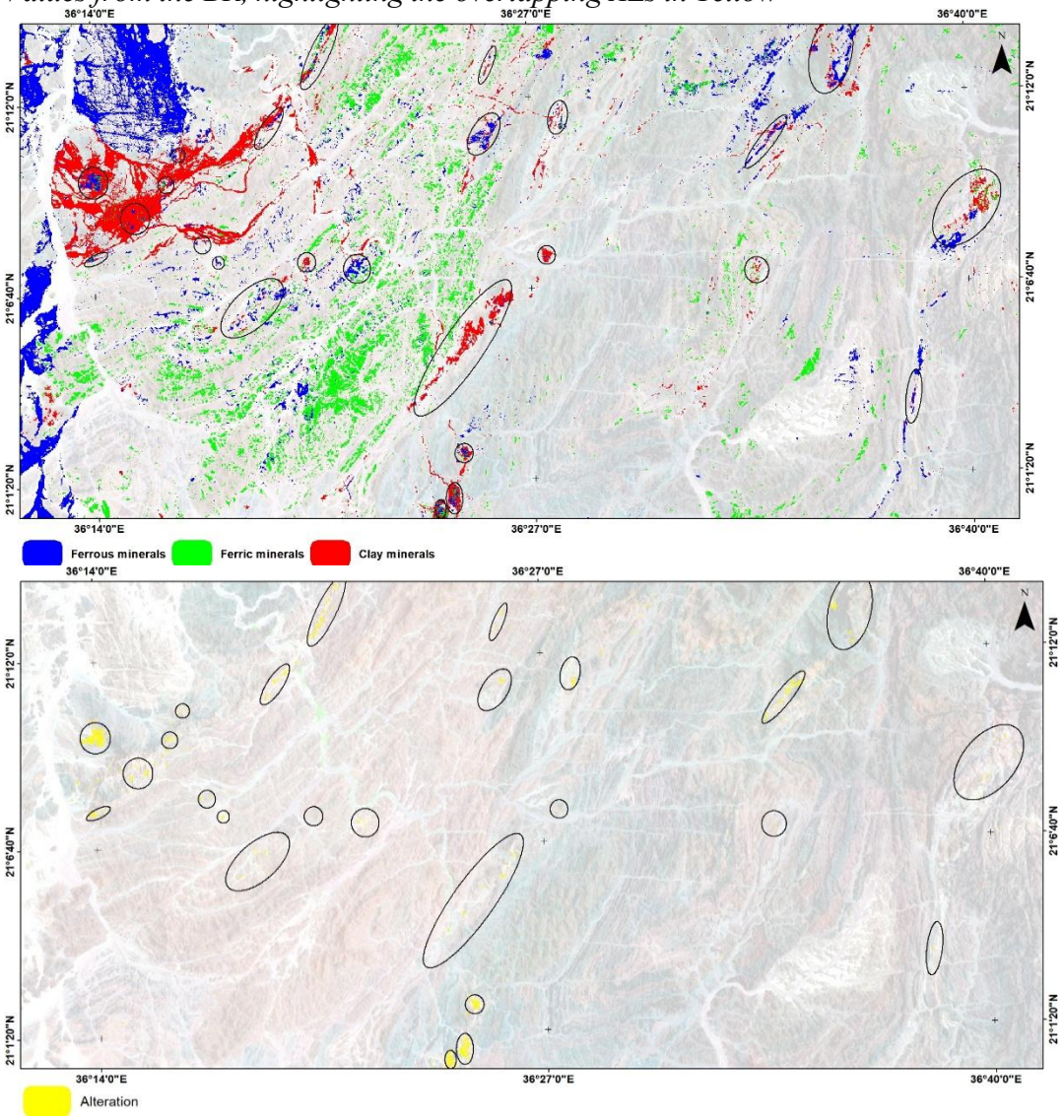

Source: Authors own elaboration

Supervised Classification

In Supervised classification using the Parallelepiped method was applied to identify HA zones in both Sabins and Crosta FCC images.

Sabins Band Ratio FCC Image

The Sabins FCC image was generated by assigning BR of 6/7, 4/6, and 4/2 to the red, green, and blue channels, respectively (Sabins and Lulla 1987). The 6/7 ratio highlights clay-rich minerals, which show high reflectance in Band 6 (SWIR1) and low reflectance in Band 7 (SWIR2), resulting in reddish hues in the composite. Areas enriched in iron oxides are emphasized by the 4/2 ratio, which exploits strong absorption in Band 2 (blue) and high reflectance in Band 4 (red), producing blue hues. The 4/6 ratio is particularly effective for mapping ferrous iron oxides and appears in green hues. Collectively, the Sabins FCC image provides a clear delineation of HA zones associated with mineralization, which are represented by crimson -orange hues (Figure 7).

Figure 7. *Sabins FCC Image showing AZs associated with Mineralization, displayed in Crimson-orange Hues; (b) Classified AZs derived from the Sabins BR Image, displayed in Red*

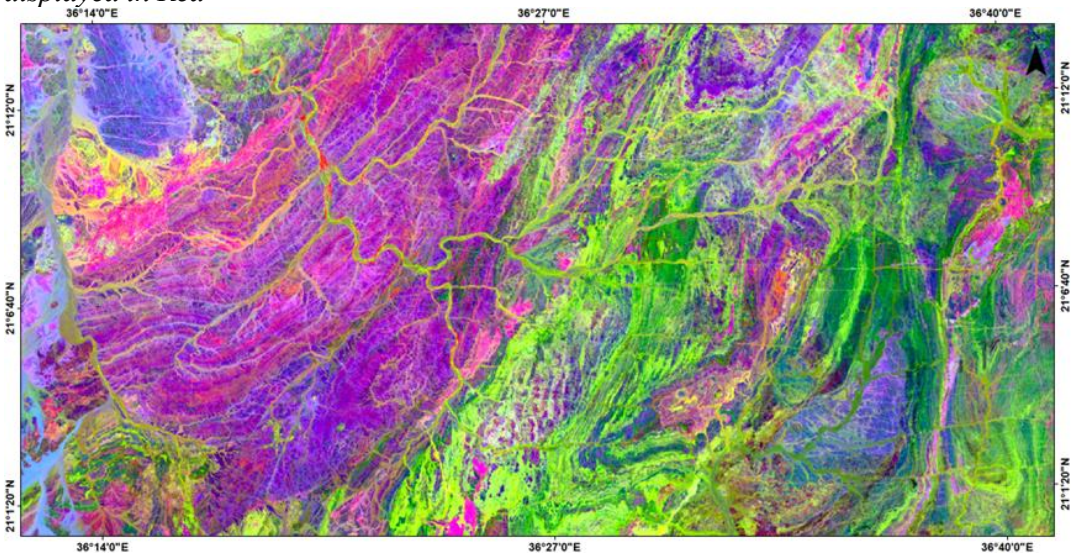

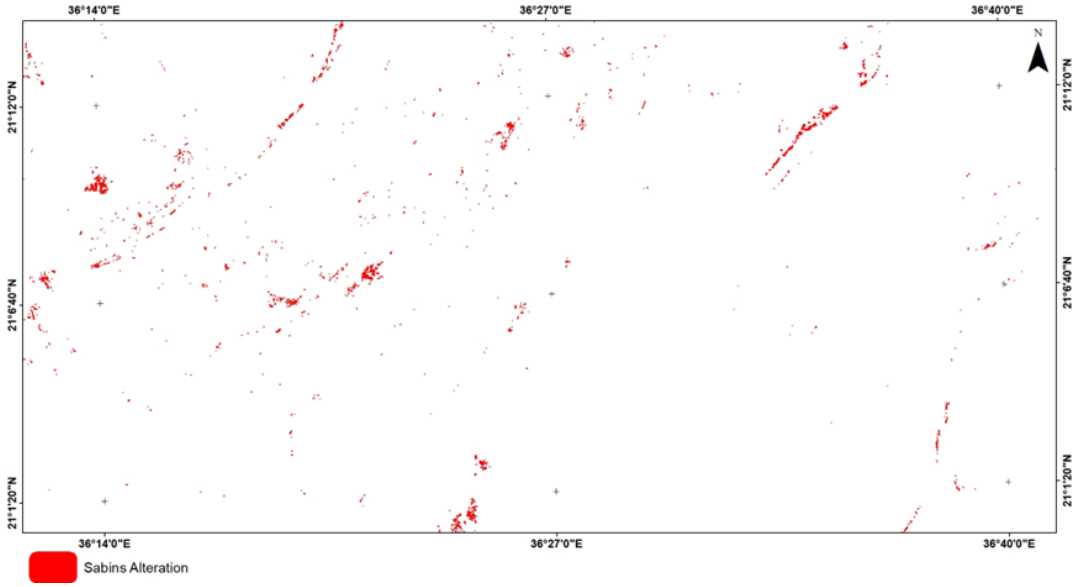

Source: Authors own elaboration

Feature Oriented Principal Component Selection (FOPCS)

FOPCS also known as the Crosta FCC method, is designed to emphasize only those spectral bands that contain diagnostic absorption features of iron oxides and clay-bearing minerals. For LC8 OLI data, the bands selected for mapping clay-bearing minerals were Bands (2, 5, 6, and 7), whereas Bands (2, 4, 5, and 7) were chosen for detecting iron oxides.

H Image (The Hydroxyl bearing and clay minerals)

The H-image is produced from principal component analysis (PCA). In general, PC1 accounts for overall albedo of the selected bands and thus contains minimal spectral variability, while PC2 reflects the contrast between the NIR and SWIR regions. In this study, eigenvector analysis (Table 1) indicated that PC3 and PC4 were the most effective components for delineating zones enriched in clay and hydroxyl-bearing minerals.

Table 2. *Eigenvector Statistics of Principal Components used for Hydroxyl-bearing Mineral mapping (H-image, FOPCS method)*

Eigenvector	Band 2	Band 5	Band 6	Band 7
PC 1	0.168356	0.432960	0.667114	0.582374
PC 2	0.463554	0.725617	-0.169314	-0.479510
PC 3	0.613774	-0.151658	-0.540803	0.554810
PC 4	0.616486	-0.512859	0.483553	-0.350851

Source: Authors own elaboration

In this case, PC4 exhibited the strongest contrast between Bands 6 and 7, with Band 6 showing a strong positive loading and Band 7 a strong negative loading. This contrast makes PC4 particularly sensitive to hydroxyl-bearing minerals. To enhance the mapping of these minerals, which appear as dark pixels in the PC4

image, the image was negated (255 - DN), followed by the application of a low-pass filter to reduce noise. The resulting processed image is referred to as the H-image.

F Image (The iron oxides rich areas)

The FOPCS transformation applied to Bands 2, 4, 5, and 7 produced the F-image. Eigenvector analysis (Table 2) indicated that either PC2 or PC4 effectively isolates iron oxide-rich zones due to the strong contrast observed among the visible bands, which is diagnostic of ferric iron minerals.

Table 3. *Eigenvector Statistics of Principal Components used for Iron Oxide mapping (F-image, FOPCS method)*

Eigenvector	Band 2	Band 4	Band 5	Band 7
PC 1	0.224696	0.476917	0.536085	0.659298
PC 2	0.312708	0.443982	0.389090	-0.744112
PC 3	0.736766	0.214905	-0.632033	0.107361
PC 4	-0.555789	0.727493	-0.402189	-0.009802

Source: Authors own elaboration

PC4 exhibited the greatest contrast in eigenvector loadings between Bands 4 and 2, making it particularly effective for mapping ferric iron oxide minerals. PC4 was therefore selected as the F-image, and a low-pass filter was applied to reduce noise, resulting in the final F-image.

The Crosta composite image (FCC) was then generated by assigning the hydroxyl-sensitive image (H-image) to the red channel, the iron oxide-sensitive image (F-image) to the blue channel, and a mathematically combined image (H-image + F-image) to the green channel. This composite effectively highlights AZs enriched in both iron oxides and clay minerals, which appear in whitish-yellow hues (Figure 8).

Figure 8. *(a) Crosta FCC Image showing AZs associated with Mineralization, displayed in Whitish - Yellow Hues; (b) Classified AZs derived from the Crosta FCC Image, displayed in Red*

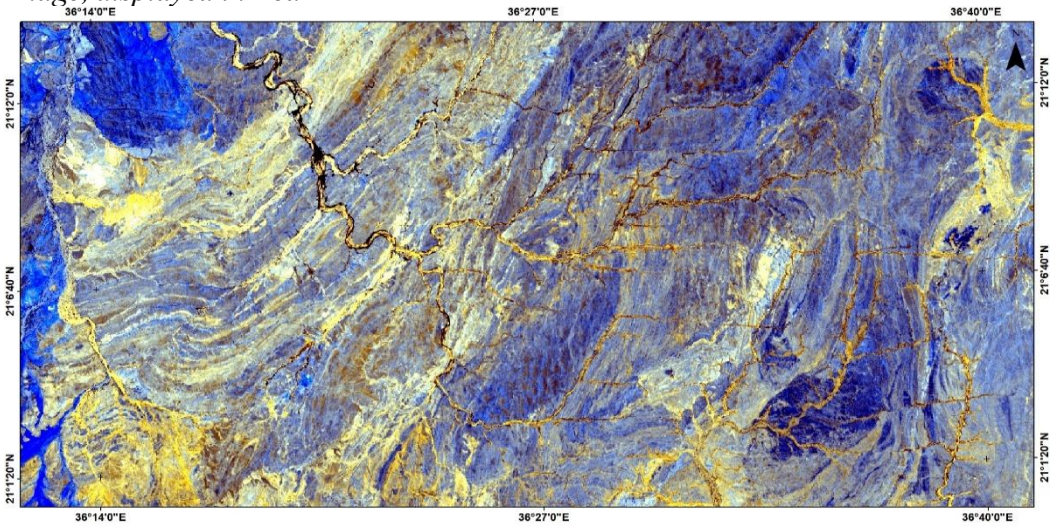

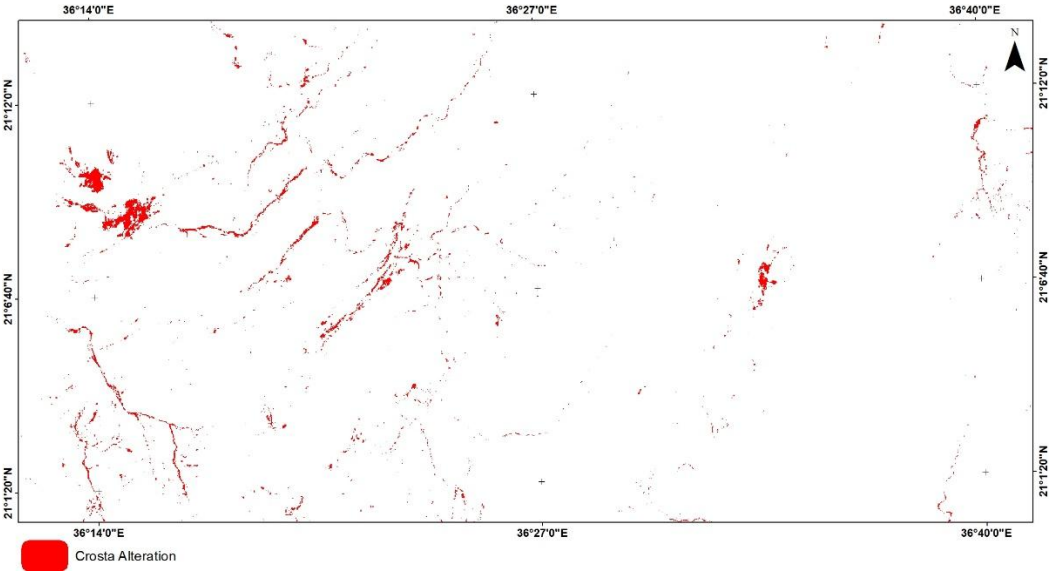

Source: Authors own elaboration

GIS Spatial Analysis

The alteration classes obtained from the supervised classification of both Sabins and Crosta composites were converted into vector format for integration within a GIS environment. A spatial intersection analysis was then performed on the vectorized AZs, enabling the delineation of highly probable AZs. These priority zones are highlighted in red in (Figure 9).

Figure 9. *(a) Classified AZs derived from the Sabins and Crosta Methods Overlaid on the FCC Image; (b) Alteration Map generated through Spatial Intersection of the Sabins and Crosta Composites, with the most probable AZs displayed in Red*

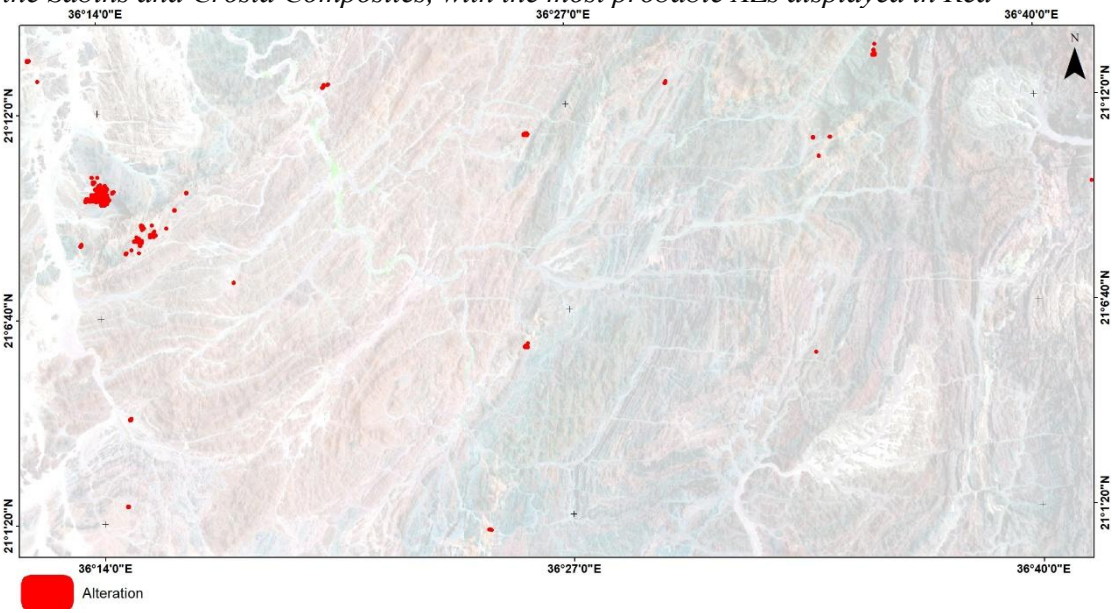

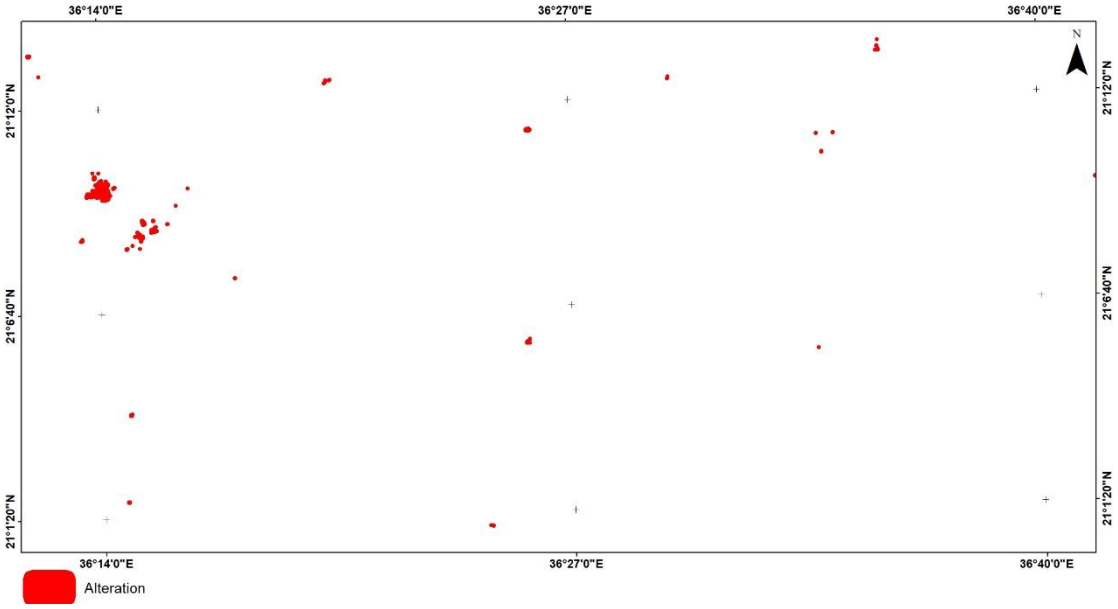

Source: Authors own elaboration

ASTER Data Processing for Mineral Prospecting

This section presents the application of two methods to AST VNIR-SWIR data for mapping hydrothermally altered minerals: (i) spectral BR indices and (ii) spectral analysis using the SAM classifier. These methods target minerals such as illite, muscovite, kaolinite, alunite, epidote, and chlorite, which display distinctive absorption and reflectance features, allowing the identification and delineation of hydro-thermal AZs, including phyllic, argillic, and propylitic zones.

Figure 10. *False Color Composite (FCC) of AST bands 4, 6, and 8 displayed in Red, Green, and Blue Channels, respectively, for the Study Area*

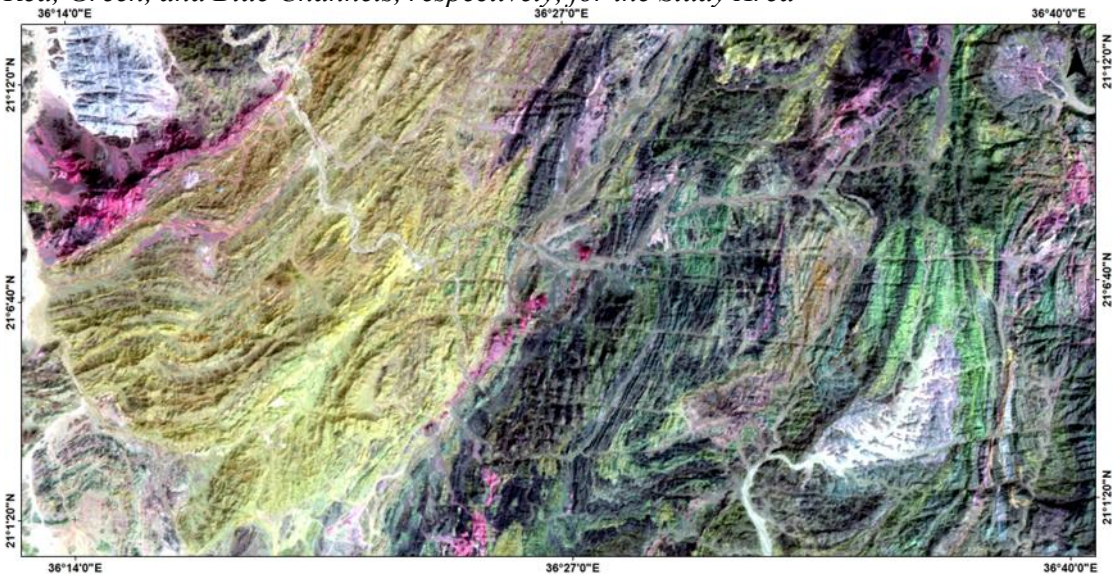

Source: Authors own elaboration

Mineral Indices

Mineral indices were derived by applying spectral BR targeting the diagnostic absorption features of selected minerals. The indices used in this study include the Muscovite Index, the Alunite Index and the Kaolinite Index.

Muscovite Mapping

The Muscovite Index highlights the absorption feature at (2.20 μm, AST Band 6), corresponding to Al-OH bearing minerals that define phyllic AZs. In the grayscale index image, muscovite-rich areas appear as bright tones, concentrated mainly in the upper left part of the study area and extending along a NNE structural trend. Additional occurrences are observed in the central lower region and near the upper right corner, The thresholded, color-coded image and its vectorized results highlight these muscovite-rich zones in red, delineating phyllic AZs (Figure 11a, b).

Alunite Mapping

The Alunite Index delineates the argillic AZs containing alunite and kaolinite minerals, which exhibit AL-O-H absorption features at (2.20 and 2.17 μm, AST band 5), respectively. The Alunite Index image shows brighter tone in the greyscale image distributed in the upper left corner of the image, the rest values are observed in the central lower part with the main NNE trend of the study area see (Figure 12 a). The thresholding high value color coded image and vectorized results appear in blue color mapping the phyllic AZs (Figure 12 b).

Kaolinite Mapping

The Kaolinite Index delineates zones enriched in kaolinite, which define argillic alteration. In the grayscale display, kaolinite-rich zones appear as bright tones, concentrated in the upper left part of the study area and extending along the NNE structural trend. Additional occurrences are observed in the central upper and lower regions and near the upper right corner, all aligned with the same structural trend. In the color-coded and vectorized image, kaolinite-rich zones are mapped in green (Figure 13a, b).

Figure 11. *Muscovite Index derived from AST Data: (a) BR image (Band 7/Band 6), highlighting Muscovite-rich Zones; (b) Vectorized Output of mapped Muscovite, displayed in Red*

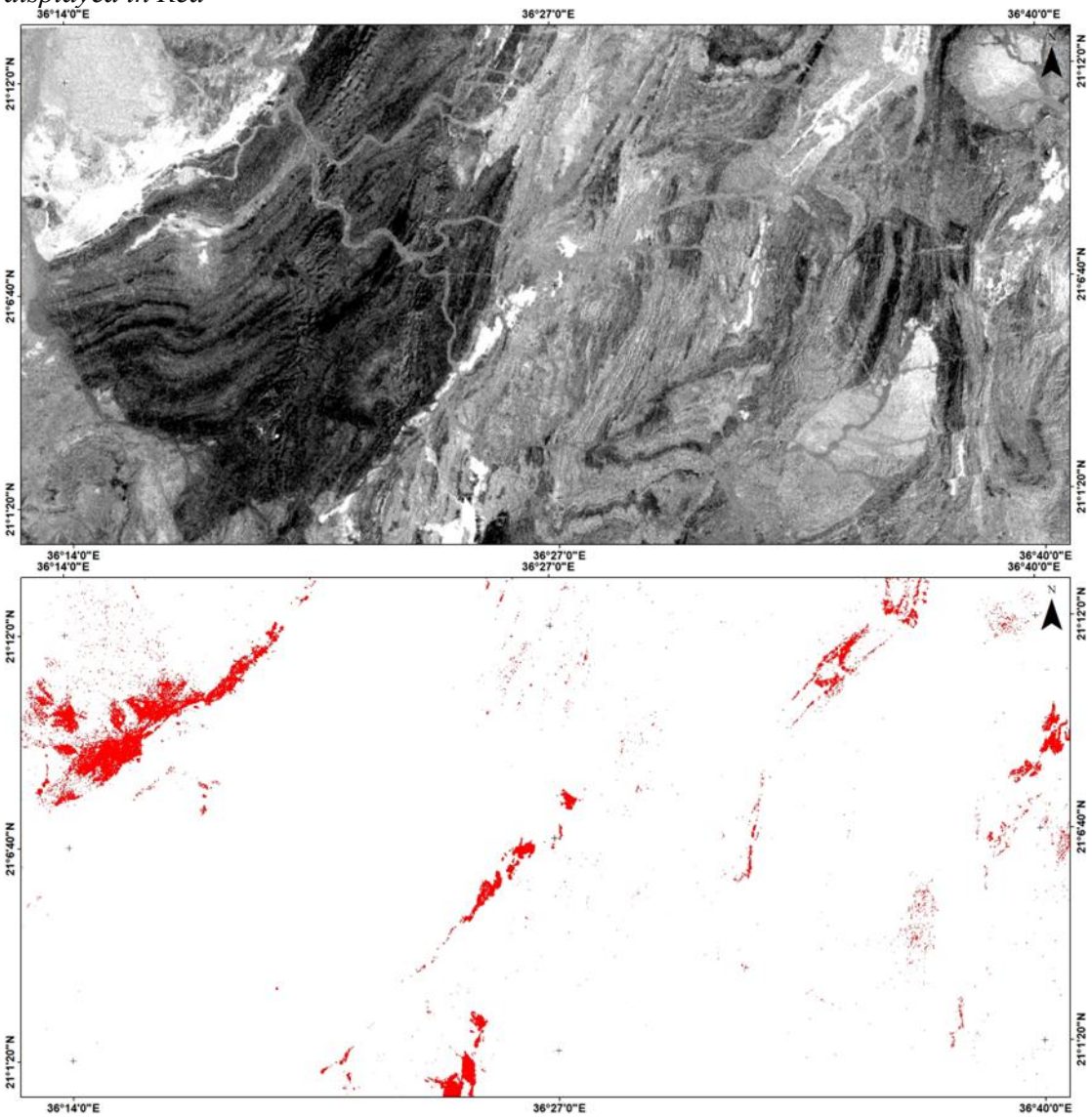

Source: Authors own elaboration

Figure 12. *Alunite Index derived from AST Data: (a) BR Image ((Band 7/Band 5) × (Band 7/Band 8)), highlighting Alunite-rich Zones; (b) Vectorized Output of mapped Alunite, displayed in Blue*

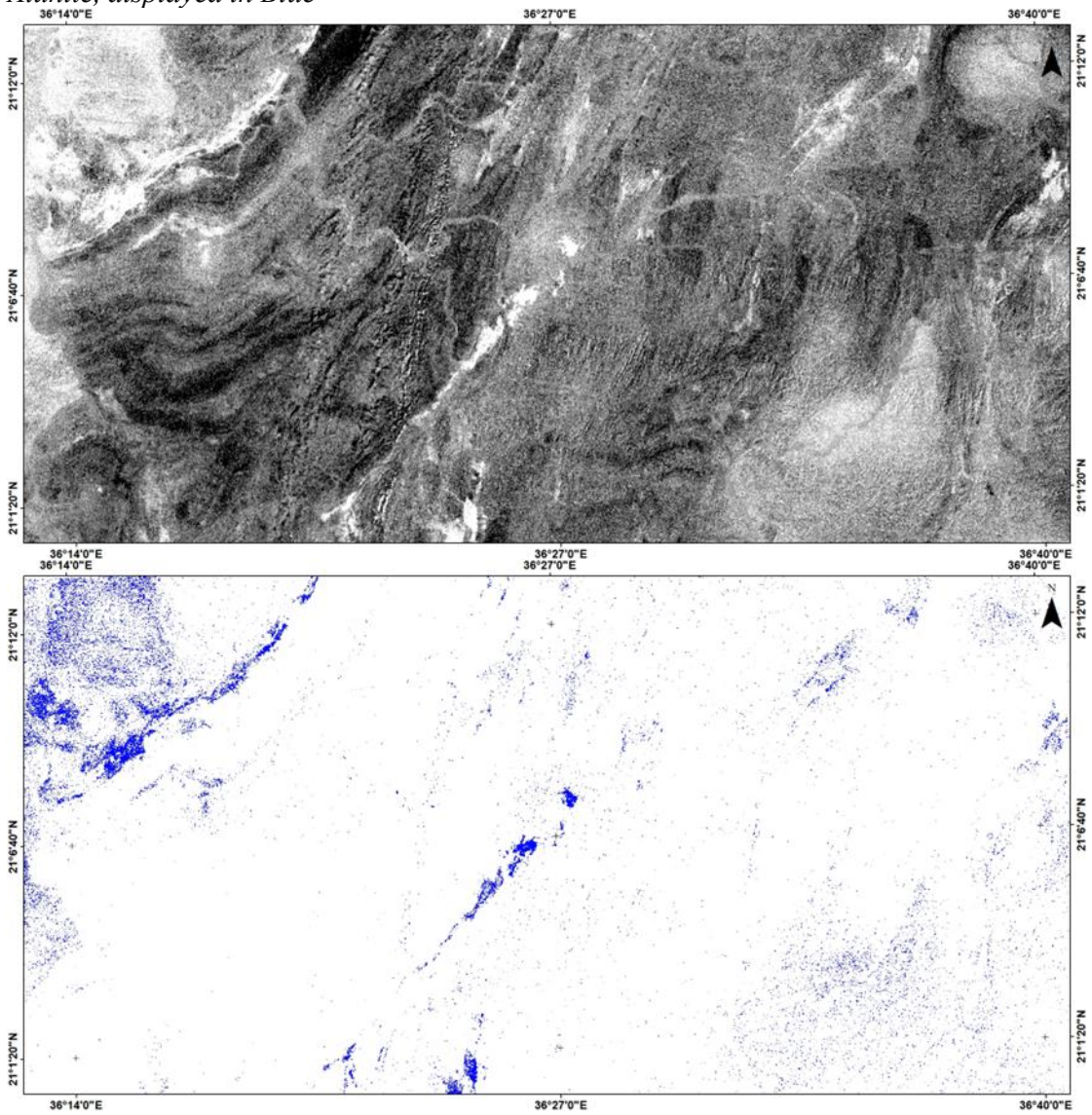

Source: Authors own elaboration

Figure 13. *Kaolinite Index derived from AST Data: (a) BR Image ((Band 4 / Band 5) × (Band 8 / Band 6)), Highlighting Kaolinite-rich Zones; (b) Vectorized Output of mapped Kaolinite, displayed in Green*

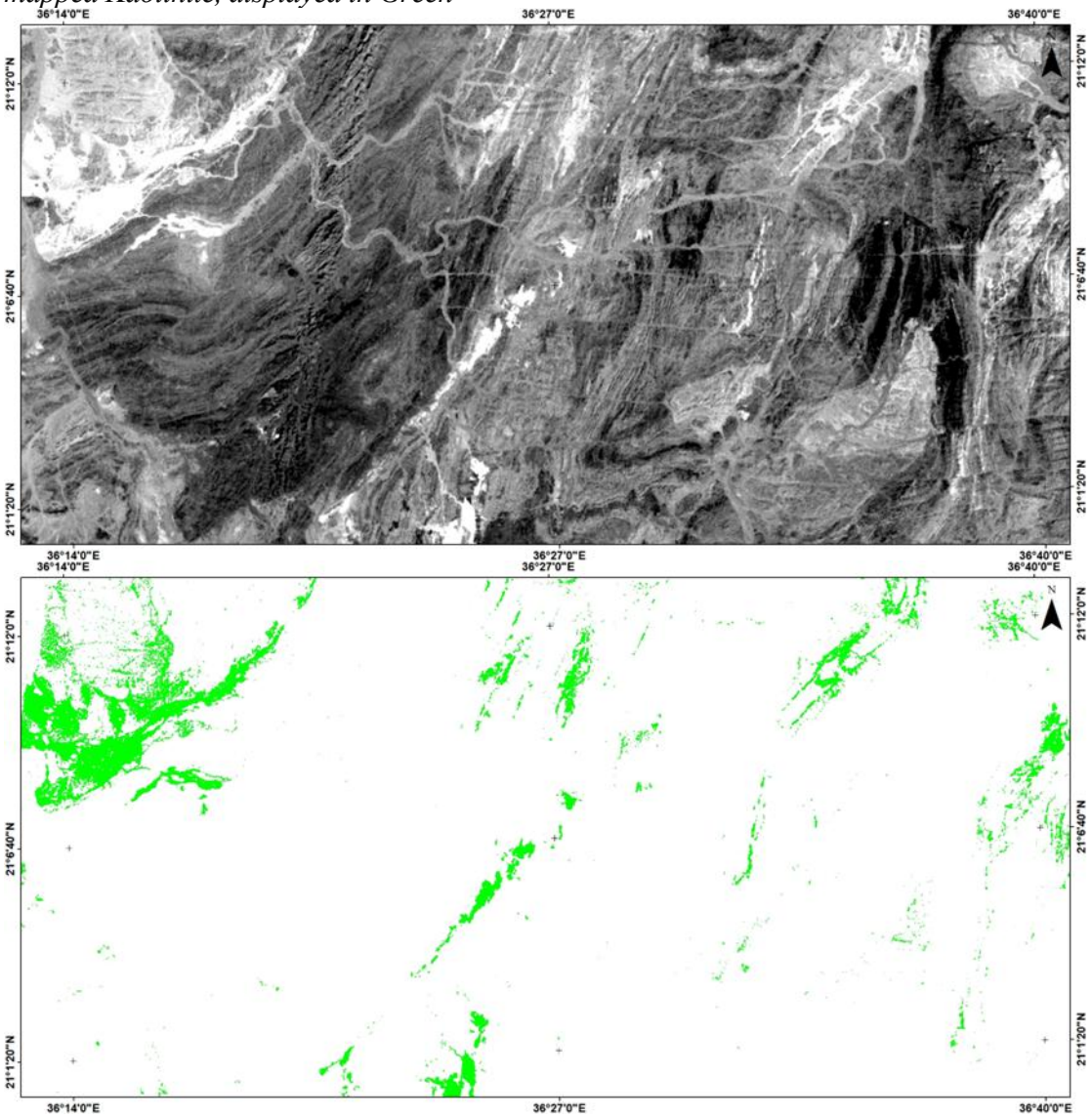

Source: Authors own elaboration

GIS Spatial Analysis

The vectorized results of the mineral indices were integrated within a GIS environment to highlight areas with overlapping phyllic and argillic AZs, which serve as indicators of potential mineralization. The analysis revealed that the upper left corner of the study area represents the most probable zone for mineralization, owing to the strong concentration of alteration signatures. Additional zones of high index values were also identified in the central lower region and near the upper right corner of the study area, all aligned with the dominant NNE structural trend (Figure 14).

Figure 14. *(a) Overlay of combined Phyllic and Argillic AZs on the FCC Image; (b) Integrated Results of Phyllic and ARGILLic AZs derived from Mineral Indices, highlighting the most probable mineralized Zones*

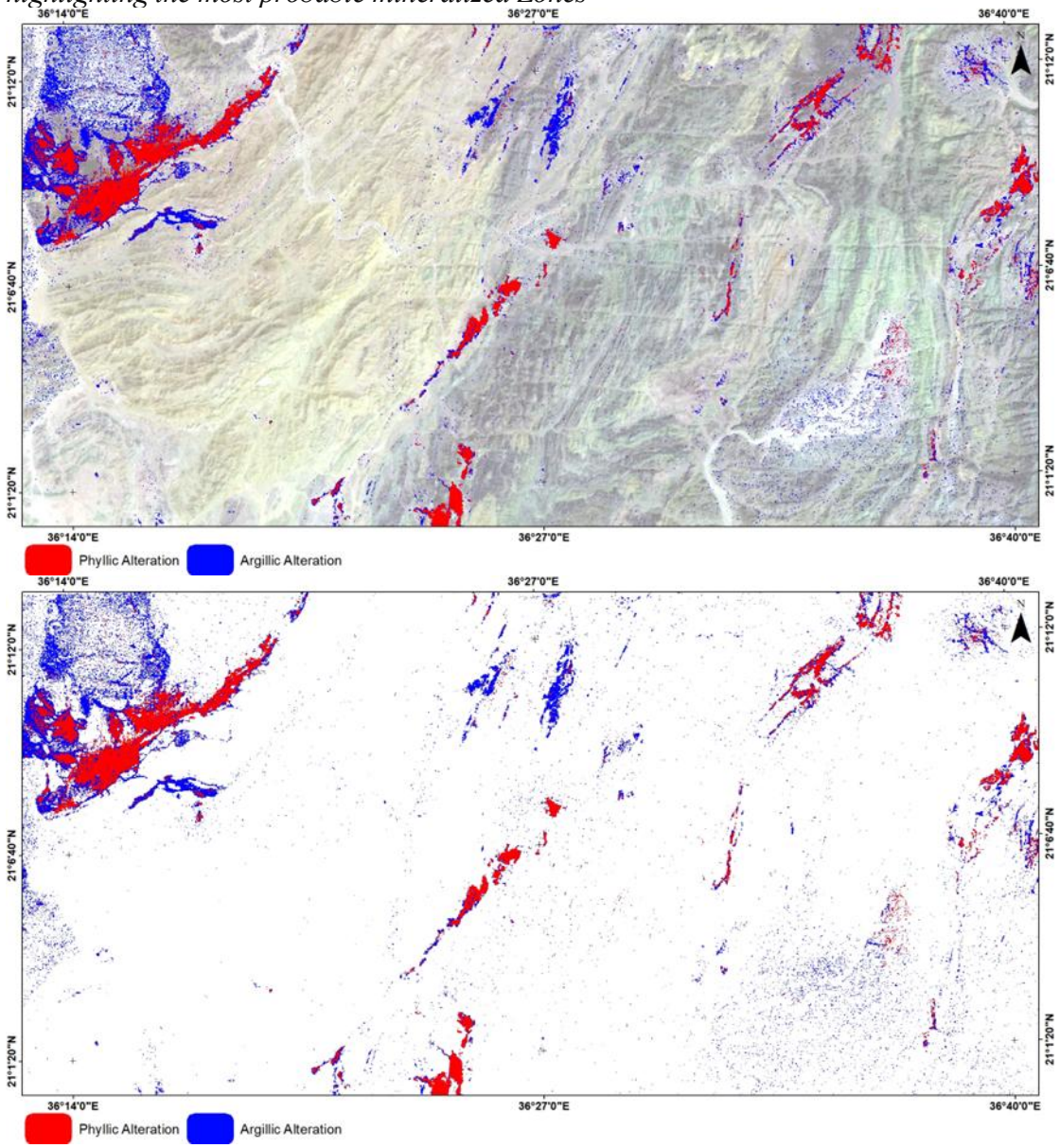

Source: Authors own elaboration

Spectral Angle Mapper Classifier

The SAM algorithm compares the spectral signature of a target object with reference spectra obtained from standardized laboratory spectral libraries, such as those provided by the USGS. In this study, spectra of common HA minerals associated with mineralization, specifically illite, muscovite, kaolinite, alunite, epidote, and chlorite, were selected from the USGS spectral library (Figure 15a). These reference spectra were subsequently resampled to match the spectral resolution and band configuration of the AST sensor (Figure 15b).

Figure 15. *(a) Laboratory Spectra of HA Minerals from the USGS Spectral Library used in this Study; (b) The Same Reference Spectra resampled to match the Spectral Resolution and Band Configuration of AST Bands*

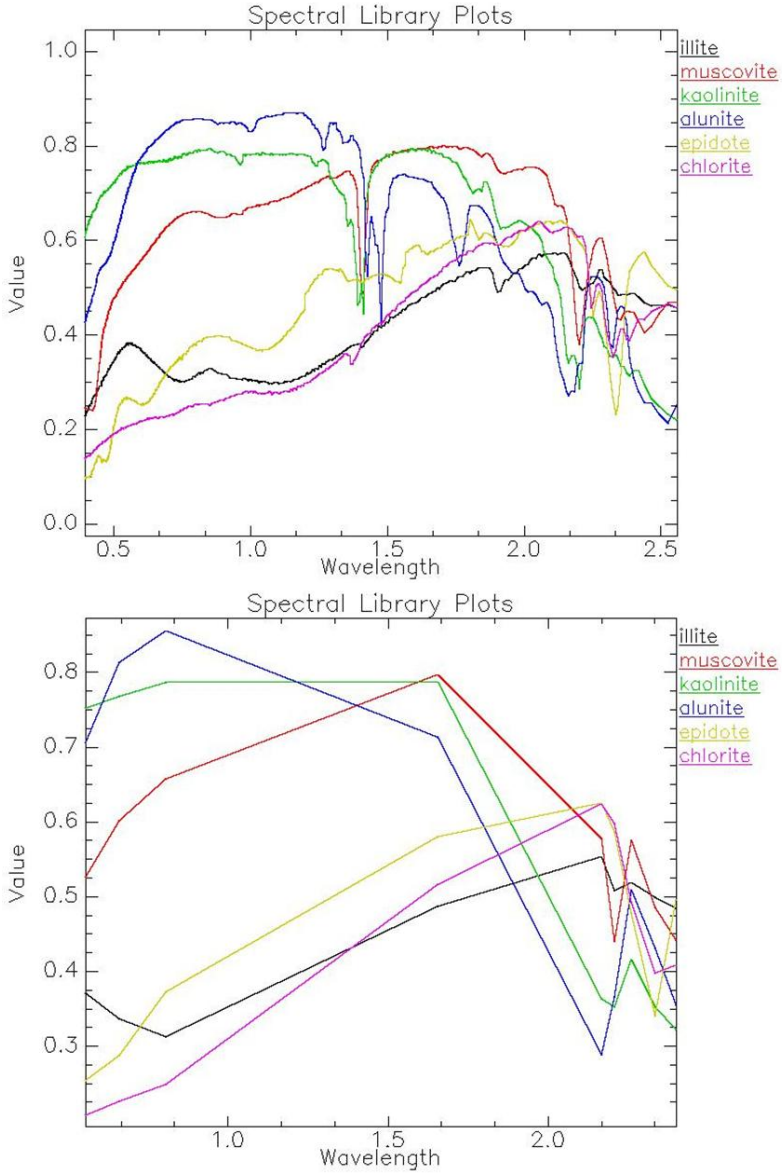

Source: Authors own elaboration

Rule images were generated to highlight the surface distribution of the selected spectra. The SAM algorithm applies a default threshold value, but in this case thresholds behave differently because lower values indicate a higher probability of a pixel belonging to the target class in the SAM rule image. Therefore, manual adjustment of the threshold was performed based on visual interpretation. The SAM-derived illite and muscovite images delineate phyllic AZs, which are represented in red. These zones are concentrated in the upper left corner of the study area and extend into the upper and central parts of the region (Figure 16).

Figure 16. *SAM classifier Results from AST data: (a) Combined Distribution of Illite and Muscovite, displayed in Red; (b) Combined Illite and Muscovite overlaid on the AST FCC Image, Highlighting Phyllic AZs in Red Hues*

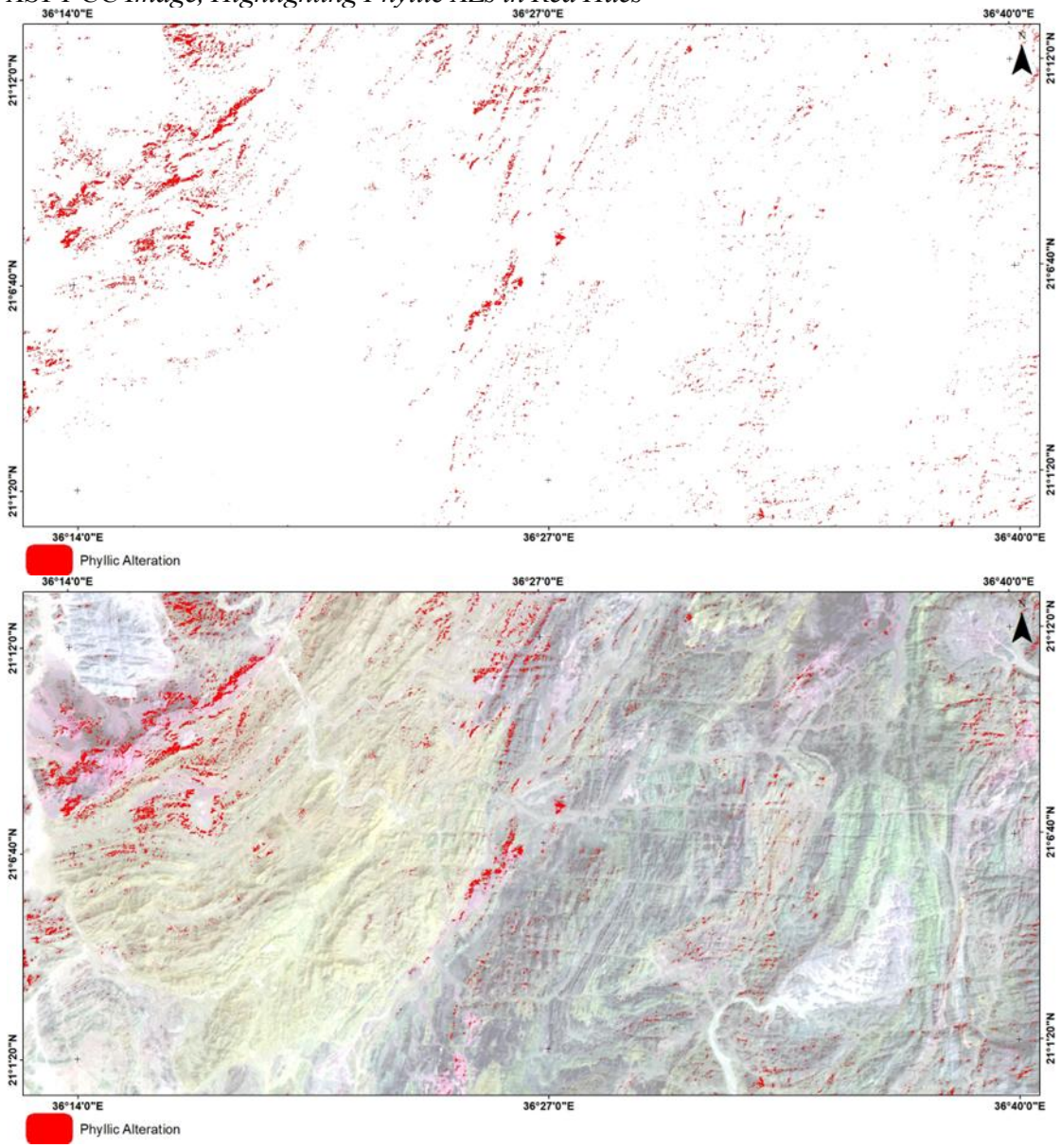

Source: Authors own elaboration

For kaolinite and alunite, the classified image highlights areas of high values corresponding to argillic AZs. These zones are represented in green and are mainly concentrated in the upper left corner of the study area, with more limited occurrences observed in the central region (Figure 17).

Figure 17. *SAM Classifier Results from AST Data: (a) Combined Distribution of Kaolinite and Alunite, Dis-played in Green; (b) Combined Kaolinite and Alunite overlaid on the AST FCC Image, Highlighting Argillic AZs in Green Hues*

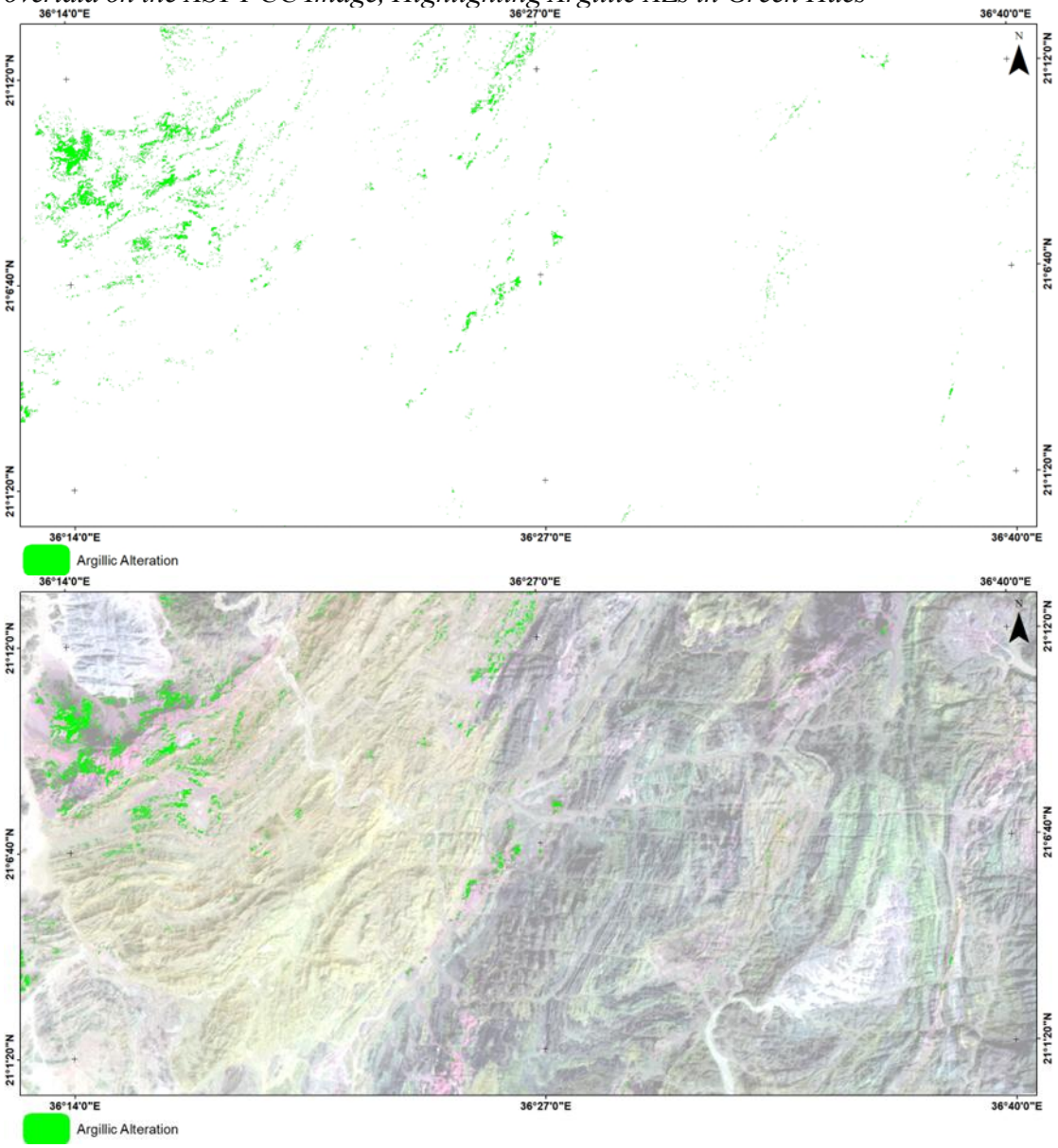

Source: Authors own elaboration

The SAM classification of epidote and chlorite was used to map propylitic AZs. These zones are represented in blue and are primarily concentrated in the left-central part of the study area (Figure 18).

Figure 18. *SAM Classifier Results from AST Data: (a) Combined Distribution of Epidote and Chlorite, displayed in Blue; (b) Combined Epidote and chlorite Overlaid on the AST FCC Image, High Lighting Propylitic AZs in Blue Hues*

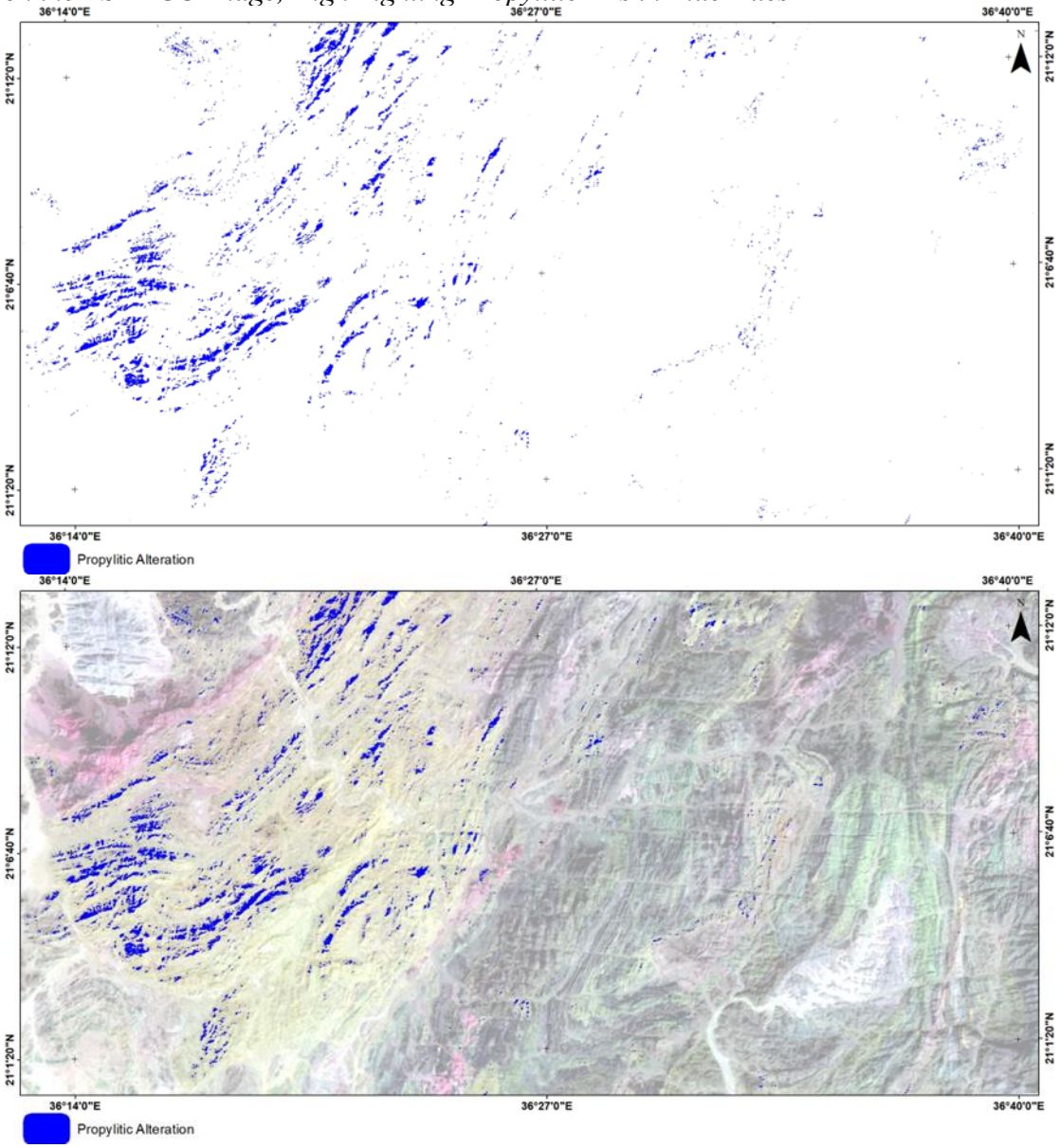

Source: Authors own elaboration

GIS Spatial Analysis

The SAM classification successfully mapped HA minerals, delineating phyllic, argillic, and propylitic zones. The resulting images illustrate the spatial distribution of these zones based on the diagnostic absorption features of their respective endmember minerals. The classified pixels were exported as shapefiles representing the extent of each alteration type. Spatial analysis was then conducted on these shapefiles to extract and delineate the most probable HA zones associated with mineralization (Figure 19a).

The results of the AST SAM spectral analysis revealed several probable AZs within the study area. These zones are primarily concentrated in the upper left corner,

aligned with a NNE structural trend, with additional occurrences in the central region and smaller, scattered zones in the upper middle part of the area (Figure 19b).

Figure 19. *Results of SAM classification applied to AST VNIR-SWIR Data: (a) Alteration Map showing Phyllic (red), Argillic (green), and Propylitic (blue) Zones; (b) AST FCC Image (bands 4, 6, and 8 in RGB) overlaid with SAM-derived AZs*

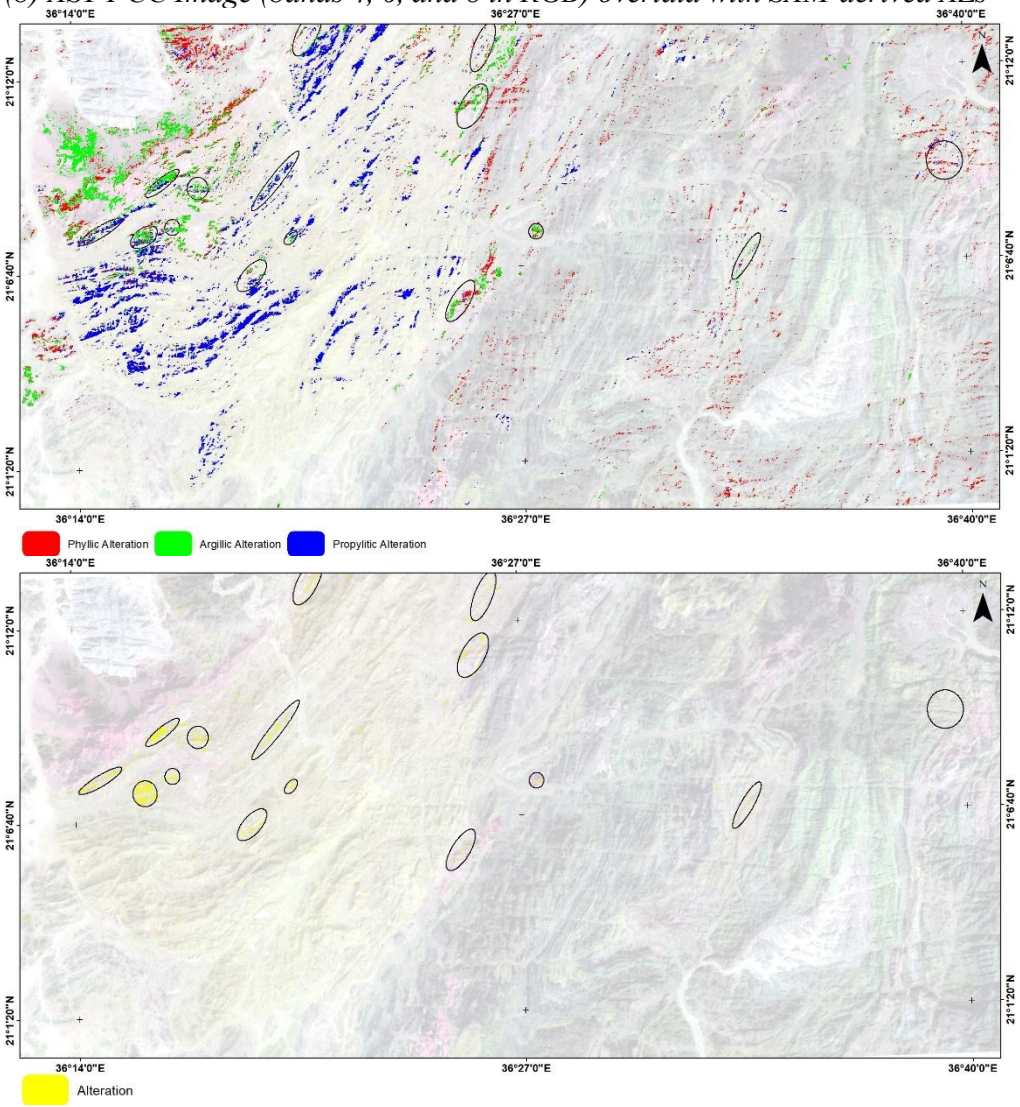

Source: Authors own elaboration

Integration of Landsat 8 and ASTER Mapping Results

LC8 includes two broad SWIR bands (band 6 and band 7) with approximate bandwidths of 0.08 µm and 0.18µm, respectively (Table 4), which limits detailed mineral discrimination. In contrast, AST acquires data in six narrower SWIR bands (bands 4 to band 9) spanning approximately 1.60 - 2.43µm, with individual bandwidths of about 0.04 - 0.10µm (Table 4), therefore, the results demonstrate that AST data provide superior capabilities for hydrothermal mineral prospecting compared to LC8 data (Figure 20).

Table 4. *Quantitative Comparative between LC8 and AST for HA Mapping Results*

Parameter	Landsat 8	ASTER	Overlap
Number of alteration zones	23	15	11
Total alteration area (km²)	53.22	20.78	
Overlap area (km²)			9.25
Percentage of combined area (%)	17.4	44.5	
Mapping scale suitability	Regional mapping	Detailed targeting	High- probable zones
Data availability	Free, frequent	Limited	
SWIR bands	2 bands	6 bands	
SWIR bandwidths	0.08 µm and 0.18µm	From 0.04 to 0.10µm	

Source: Authors own elaboration, bands specifications from USGS and NASA documentation

Quantitative comparison indicates that LC8 delineated 23 AZs covering approximately 53.22 km², whereas AST identified 15 more spatially restricted zones covering about 20.78 km². Spatial intersection analysis reveals 11 overlapping zones with a total area of 9.25 km², corresponding to approximately 44.5 % of the AST-derived alteration area and 17.4 % of the LC8-derived area. These intersected zones served as the most prospective areas (Figure 20b).

Figure 20. *AZs Maps (a) probable AZs related to Mineralization delineated from LC8 and AST Data; (b) The AZs related to Mineralization delineated from the Spatial Intersection*

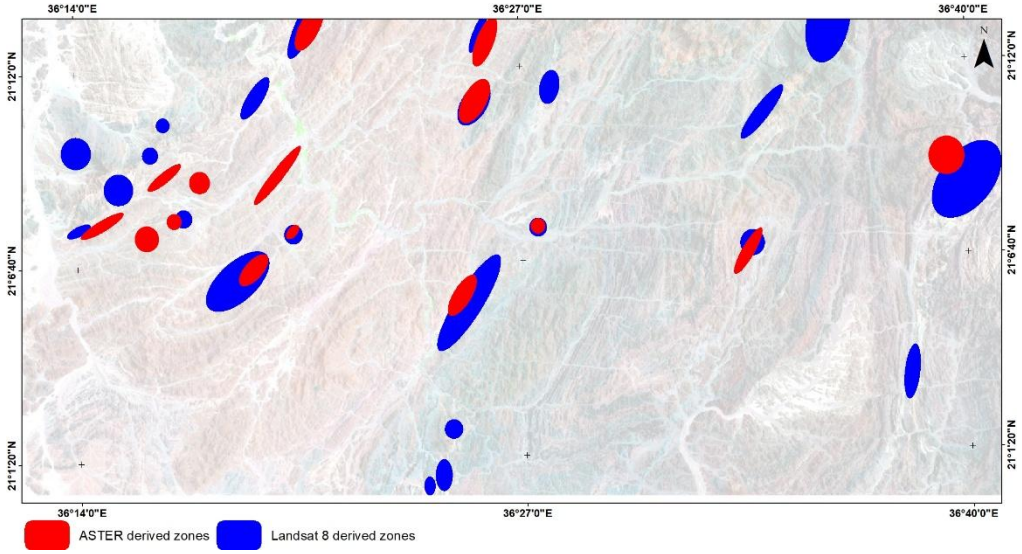

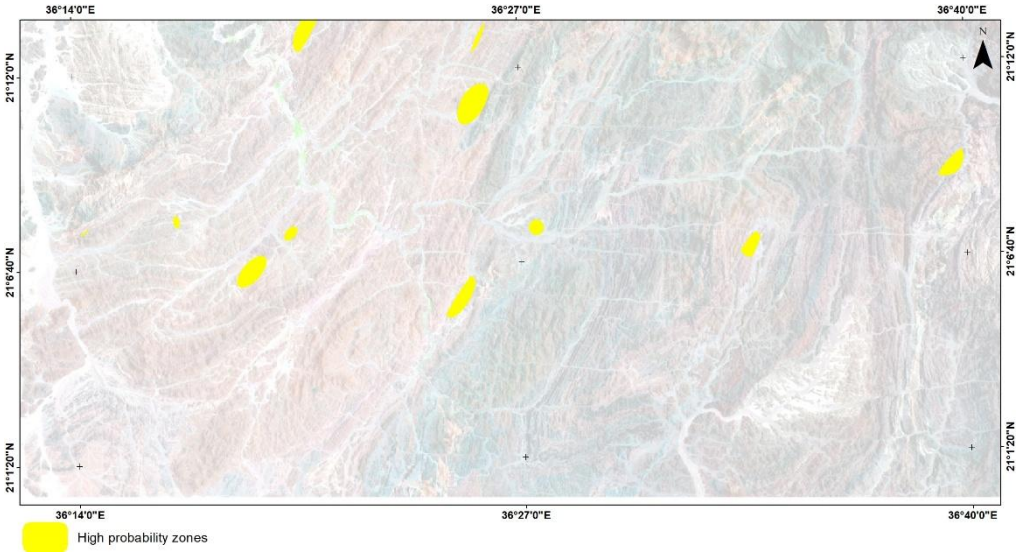

Source: Authors own elaboration

Discussion

The spectral characteristics of HA zones were investigated using integrated LC8 OLI and AST datasets, applying BR analysis, the Crosta technique, supervised classification, mineral indices, and the SAM (SAM) classifier. The integration of these complementary approaches within a GIS framework enabled robust delineation of the most prospective HA zones across the study area.

Overall, the results a quantitative comparison between LC8 and AST datasets (Table 4) indicates that AST-derived AZs overlap approximately 44.5 % of the AST area and 17.4 % of the Landsat area, highlighting the broader reconnaissance capability of Landsat and the more selective mineral discrimination achieved using AST enables the separation of diagnostic absorption minerals such as muscovite, kaolinite, alunite, chlorite, and epidote, resulting in more precise mapping of phyllic, argillic, and propylitic AZs (Figure 19). Accordingly, AST represents a valuable tool for the early stages of mineral exploration, offering a rapid, cost-effective, and reliable approach for identifying prospective zones associated with HA minerals.

Structurally, the mapped AZs which associated with dominant NNE-trending lineaments, fault systems, and shear zones that correspond with regional structural of the ANS. These structures, formed during late Neoproterozoic tectonic events, and recognized for their role in controlling hydrothermal fluid flow. Therefore, AZs that follow these NNE-trending structural were regarded as most probable zones.

Given logistical constraints, limited accessibility in the rugged terrain of the RSHs and the lack of available published geological data in the study area, the interpretation and accuracy assessment of this study relies on the spectral characteristics of satellite imagery, in the absence of field-based validation. Although Landsat-8 and AST data are widely recognized and well documented for HA mapping, future ground verification would substantially improve the reliability of the results. Integrating remote sensing outputs with geophysical data like (magnetic and radiometric surveys)

together with structure and geochemical analyses, would enhance confidence in delineating HA zones and assessing mineralization potential in the study area.

Finally, the differences observed among the applied image processing techniques underscore the importance of using complementary approaches. BR methods emphasize specific spectral contrasts like ferrous oxide, ferric oxide and clay/hydroxyl-bearing (Figure 6a), mineral indices target diagnostic absorption features for muscovite, alunite and kaolinite indices for mapping the altered zones (Figure 14), and SAM classification relies on spectral similarity to reference libraries (Figure 15), to delineating phyllic, argillic, and propylitic zones (Figure 14). Consequently, each method highlights different aspects of HA, and discrepancies among results are expected. However, their integration within a GIS framework provides a more probable and reliable interpretation than dependence on single technique.

Conclusions

This study reveals the effective of the integrated LC8 and AST data for HA mapping around in the RSHs, NE Sudan.

Exploration targets were classified based on the correspond closely with regional structural controls on mineralization within the study area, Gebeit Terrane within the ANS. The results highlight NNE-trending structures as high-priority exploration targets (Figure 19), representing the most prospective zones, whereas the remaining anomalies are considered secondary targets suitable for regional-scale reconnaissance.

Quantitative analysis shows that AST derived AZs overlap approximately 44.5% of the AST area and 17.4 % of the LC8 area, defining high-confidence targets where both sensors agree (Figure 20). These intersected zones represent the most prospective areas for pre-filed exploration stage, confirming that combined use of LC8 and AST offers a robust, cost-effective workflow for mineral exploration in arid and inaccessible.

Future research should focus on integrating alteration mapping with hyperspectral satellite data which offers spectrally narrower bands and very high spatial resolution, together with high-resolution structural data to enable detailed analysis of structure-controlled mineralization. Expanding this methodology through field sampling, and integration with geophysical datasets, including spectroradiometer measurements and magnetic, to enhance resulting accuracy.

References

Abdelsalam MG, Robinson C, El-Baz F, Stern RJ (2000) Applications of orbital imaging radar for geologic studies in arid regions: The Saharan testimony. *Photogrammetric Engineering & Remote Sensing* 66(6): 717–726.

Abdelsalam MG (2010) Quantifying 3D post-accretionary tectonic strain in the Arabian–Nubian Shield: Superimposition of the Oko shear zone on the Nakasib suture, Red Sea Hills, Sudan. *Journal of African Earth Sciences* 56(4–5): 167–178.

Abrams M, Hook S, Ramachandran B (2002) *ASTER user handbook*, version 2. Jet Propulsion Laboratory, Pasadena, CA.

Abrams M (2000) The Advanced Spaceborne Thermal Emission and Reflection Radiometer (ASTER): Data products for the high spatial resolution imager on NASA's Terra platform. *International Journal of Remote Sensing* 21(5): 847–859.

Alimohammadi M, Alirezaei S, Kontak DJ (2015) Application of ASTER data for exploration of porphyry copper deposits: A case study of the Daraloo–Sarmeshk area, southern Kerman copper belt, Iran. *Ore Geology Reviews* 70: 290–304.

Almond DC, Ahmed F (1987) Ductile shear zones in the northern Red Sea Hills, Sudan, and their implication for crustal collision. *Geological Journal* 22(S2): 175–184.

Amer R, El Mezayen A, Hasanein M (2016) ASTER spectral analysis for alteration minerals associated with gold mineralization. *Ore Geology Reviews* 75: 239–251.

Berger BR, Mars JL, Denning P, Phillips JD, Hammarstrom JM, Zientek ML, Dicken CL, Drew LJ, Seltmann R, Herrington RJ (2014) *Porphyry copper assessment of western Central Asia*. U.S. Geological Survey, Reston, VA.

Blondes MS, Gans KD, Thordsen JJ, Reidy ME, Thomas B, Engle MA, Kharaka YK, Rowan EL (2016) *US Geological Survey National Produced Waters Geochemical Database v2.3 (provisional)*. U.S. Geological Survey.

Carrino TA, Crósta AP, Toledo CL, Silva AM, Silva JL (2015) Geology and hydrothermal alteration of the Chapi Chiara prospect and nearby targets, southern Peru, using ASTER data and reflectance spectroscopy. *Economic Geology* 110(1): 73–90.

Cooley T, Anderson GP, Felde GW, Hoke ML, Ratkowski AJ, Chetwynd JH, Gardner JA, Adler-Golden SM, Matthew MW, Berk A, Bernstein LS (2002) FLAASH, a MODTRAN4-based atmospheric correction algorithm: Application and validation. In: *Proceedings of the IEEE International Geoscience and Remote Sensing Symposium*, vol. 3, pp. 1414–1418.

Crósta AP, De Souza Filho CR, Azevedo F, Brodie C (2003) Targeting key alteration minerals in epithermal deposits in Patagonia, Argentina, using ASTER imagery and principal component analysis. *International Journal of Remote Sensing* 24(21): 4233–4240.

Crósta AP, Moore J (1989) *Enhancement of Landsat Thematic Mapper imagery for residual soil mapping in SW Minas Gerais State, Brazil: A prospecting case history in greenstone belt terrain.* In: Proceedings of the Seventh Thematic Conference on Remote Sensing for Exploration Geology, Calgary, Canada, pp. 1173–1187.

Debba P, Van Ruitenbeek FJ, Van der Meer FD, Carranza EJ, Stein A (2005) Optimal field sampling for targeting minerals using hyperspectral data. *Remote Sensing of Environment* 99(4): 373–386.

El Khidir SO, Babikir IA (2013) Digital image processing and geospatial analysis of Landsat 7 ETM+ for mineral exploration, Abidiya area, North Sudan. *International Journal of Geomatics and Geosciences* 3(3): 645–658.

El Khidir SOH (2006) *Remote sensing and GIS applications in geological mapping, prospecting for mineral deposits and groundwater: Berber sheet area, northern Sudan*. PhD dissertation, Al Neelain University.

Fitches WR, Graham RH, Hussein IM, Ries AC, Shackleton RM, Price RC (1983) The late Proterozoic ophiolite of Sol Hamed, NE Sudan. *Precambrian Research* 19(4): 385–411.

Fraser SJ, Green AA (1987) A software defoliant for geological analysis of band ratios. *International Journal of Remote Sensing* 8(3): 525–532.

Gupta RP (2017) *Remote sensing geology*. Springer, Berlin.

Hunt GR, Ashley RP (1979) Spectra of altered rocks in the visible and near infrared. *Economic Geology* 74(7): 1613–1629.

Hunt GR (1979) Near-infrared (1.3–2.4 μm) spectra of alteration minerals: Potential for use in remote sensing. *Geophysics* 44(12): 1974–1986.

Johnson PR, Andresen A, Collins AS, Fowler AR, Fritz H, Ghebreab W, Kusky T, Stern RJ (2011) Late Cryogenian–Ediacaran history of the Arabian–Nubian Shield. *Journal of African Earth Sciences* 61(3): 167–232.

Johnson PR, Kattan FH, Al-Saleh AM (2004) Neoproterozoic ophiolites in the Arabian Shield: Field relations and structure. *Developments in Precambrian Geology* 13: 129–162.

Klemenic PM, Poole S (1988) The geology and geochemistry of Upper Proterozoic granitoids from the Red Sea Hills, Sudan. *Journal of the Geological Society* 145(4): 635–643.

Kröner A, Greiling R, Reischmann T, Hussein IM, Stern RJ, Dürr S, Krüger J, Zimmer M (1987) Pan-African crustal evolution in the Nubian segment of northeast Africa. In: *Proterozoic Lithospheric Evolution*, vol. 17, pp. 235–257.

Kruse FA, Lefkoff AB, Boardman JW, Heidebrecht KB, Shapiro AT, Barloon PJ, Goetz AF (1993) The spectral image processing system (SIPS). *Remote Sensing of Environment* 44(2–3): 145–163.

Lillesand T, Kiefer RW, Chipman J (2015) *Remote sensing and image interpretation*. Wiley, New York.

Loughlin WP (1991) Principal component analysis for alteration mapping. *Photogrammetric Engineering & Remote Sensing* 57(9): 1163–1169.

Mars JC, Rowan LC (2006) Regional mapping of phyllic- and argillic-altered rocks using ASTER data. *Geosphere* 2(3): 161–186.

Mwaniki MW, Möller MS, Schellmann G (2015) A comparison of Landsat 8 and Landsat 7 in mapping geology and visualising lineaments. *ISPRS Archives* 40: 897–903.

Ninomiya Y (2003) A stabilized vegetation index and mineralogic indices for ASTER data. In: *IGARSS 2003 Proceedings*, vol. 3, pp. 1552–1554.

Pour AB, Hashim M (2012) Identifying areas of high economic-potential copper mineralization using ASTER data. *Advances in Space Research* 49(4): 753–769.

Pour AB, Hashim M (2012) The application of ASTER data to porphyry copper and epithermal gold deposits. *Ore Geology Reviews* 44: 1–9.

Pour AB, Hashim M, Park Y, Hong JK (2018) Mapping alteration mineral zones using ASTER data. *Geocarto International* 33(12): 1281–1306.

Pour AB, Hashim M, Hong JK, Park Y (2019) Lithological and alteration mineral mapping using Landsat-8 and ASTER data. *Ore Geology Reviews* 108: 112–133.

Rajendran S, Nasir S, Kusky TM, Ghulam A, Gabr S, El-Ghali MA (2013) Detection of hydrothermal mineralized zones using ASTER data. *Ore Geology Reviews* 53: 470–488.

Richards JA (2022) *Remote sensing digital image analysis*. Springer, Berlin.

Rowan LC, Hook SJ, Abrams MJ, Mars JC (2003) Mapping hydrothermally altered rocks using ASTER. *Economic Geology* 98(5): 1019–1027.

Rowan LC, Mars JC (2003) Lithologic mapping using ASTER data. *Remote Sensing of Environment* 84(3): 350–366.

Roy DP, Wulder MA, Loveland TR et al. (2014) Landsat-8: Science and product vision. *Remote Sensing of Environment* 145: 154–172.

Sabins FF (1999) Remote sensing for mineral exploration. *Ore Geology Reviews* 14(3–4): 157–183.

Sabins FF Jr, Lulla K (1987) *Remote sensing: Principles and interpretation*. W.H. Freeman, New York.

Safari M, Maghsoudi A, Pour AB (2018) Application of Landsat-8 and ASTER data for porphyry copper exploration. *Geocarto International* 33(11): 1186–1201.

Seedorff E, Dilles JH, Proffett JM, Einaudi MT, Zurcher L, Stavast WJ, Johnson DA, Barton MD (2005) *Porphyry deposits: Characteristics and origin of hypogene features.* Economic Geology 100th Anniversary Volume: 251–298.

Shnain SK, Najm MN, Taher NA, Abdalrazzaq AS, Rashit B, Lishchyna V (2024) *Classification of Landsat 8 images using CNN based on MNF transform.* In: Proceedings of the 35th FRUCT Conference, pp. 692–698.

Spatz DM, Wilson RT, Pierce FW, Bolm JG (1995) Remote sensing characteristics of porphyry copper systems. *Arizona Geological Society Digest* 20: 94–108.

Stern RJ (1994) Arc assembly and continental collision in the Neoproterozoic African Orogen. *Annual Review of Earth and Planetary Sciences* 22: 319–351.

Stern RJ (2002) Crustal evolution in the East African Orogen. *Journal of African Earth Sciences* 34(3–4): 109–117.

Testa FJ, Villanueva C, Cooke DR, Zhang L (2018) Lithological and hydrothermal alteration mapping using ASTER imagery. *Remote Sensing* 10(2): 203.

Vail JR (1985) Alkaline ring complexes in Sudan. *Journal of African Earth Sciences* 3(1–2): 51–59.

Van der Meer FD, Van der Werff HM, Van Ruitenbeek FJ et al. (2012) Multi-and hyperspectral geologic remote sensing: A review. *International Journal of Applied Earth Observation and Geoinformation* 14(1): 112–128.

Wulder MA, White JC, Goward SN et al. (2008) Landsat continuity: Issues and opportunities. *Remote Sensing of Environment* 112(3): 955–969.

Yamaguchi Y, Fujisada H, Kahle AB et al. (2001) ASTER instrument performance and applications. In: *IGARSS 2001 Proceedings*, vol. 3, pp. 1215–1216.

Yamaguchi Y, Fujisada H, Kudoh M et al. (1999) ASTER instrument characterization. *Advances in Space Research* 23(8): 1415–1425.

Zeinelabdein KE, Albiely A (2008) Ratio image processing techniques for mineral prospecting. *ISPRS Archives* 37: 1295–1298.

Zhang X, Pazner M, Duke N (2007) Lithologic and mineral information extraction using ASTER data. *ISPRS Journal of Photogrammetry and Remote Sensing* 62(4): 271–282.

Abbreviations

Abbreviations used in this paper include:

OLI	Operational Land Imager
Landsat 8	LC8
ASTER	AST
Red Sea Hills	RSHs
ANS	Arabian Nubian Shield
VNIR	Visible / Near Infrared
SWIR	Shortwave Infrared
TIR	Thermal Infrared
TIRS	Thermal Infrared Sensor
USGS	United State Geological Survey
UTM	Universal Transverse Mercator
Band Ratio	BR
Hydrothermal Alteration	HA
Alteration Zones	AZs
WGS	World Geodetic System
ENVI	Environment for Visualizing Images
FLAASH	Fast Line of sight Atmospheric Analysis of Spectral Hypercube
MNF	Minimum Noise Fraction
FOPCS	Feature Oriented Principal Component Selection
PCA	Principal Component Analysis
DN	Digital Number
ROI	Regions Of Interest
FCC	False Color Composite
NNE	North Northeast
SSW	South Southwest
SAM	Spectral Angle Mapper